THESIS

VISUAL HULL METHOD FOR REALISTIC 3D PARTICLE SHAPE RECONSTRUCTION BASED ON HIGH-RESOLUTION PHOTOGRAPHS OF SNOWFLAKES IN FREEFALL FROM MULTIPLE VIEWS

Submitted by

Cameron Kleinkort

Department of Electrical and Computer Engineering

In partial fulfillment of the requirements

For the Degree of Master of Science

Colorado State University

Fort Collins, Colorado

Summer 2016

Master's Committee:

Advisor: Branislav Notaros

V. N. Bringi
Steven Rutledge
Ali Pezeshki

ABSTRACT

VISUAL HULL METHOD FOR REALISTIC 3D PARTICLE SHAPE RECONSTRUCTION BASED ON HIGH-RESOLUTION PHOTOGRAPHS OF SNOWFLAKES IN FREEFALL FROM MULTIPLE VIEWS

Proposed and presented is a visual hull method and technique for reconstruction of realistic 3D shapes of snowflakes and other hydrometeors based on high-resolution photographs of particles in freefall from multiple views captured by a multi-angle snowflake camera (MASC), or another similar instrument. The visual hull of an object is the maximal domain that gives the same silhouettes as the object from a certain set of viewpoints. From the measured fall speed and the particle shape reconstruction, the particle density and dielectric constant are estimated. This is the first time accurate realistic shape reconstructions based on high-resolution photographs of real (measured) snowflakes are performed. The results are clearly much better than any similar data in the literature. They demonstrate – in experiments involved in real snow storm observations and those with simulated and fake 3D printed snowflakes – sufficient silhouette information from the five cameras of the expanded MASC system and excellent performance of the implemented mechanical calibration and software self-calibration of the system. In addition to enabling realistic "particle-by-particle" computations of polarimetric radar measurables for winter precipitation, the visual hull 3D shape reconstructions of hydrometeors can be used for microphysical characteristics analyses, hydrometeor classification, and improvement of radar-based estimations of liquid equivalent snow rates.

ACKNOWLEDGEMENTS

I would first like to acknowledge my advisor Dr. Branislav Notaros for his unparalleled support and guidance throughout my time at Colorado State University. I would also like to acknowledge Gwo-Jong Huang for his invaluable work on this project, for always answering any questions I had, and for his time spent explaining concepts to me in an easy to understand way. I would also like to thank the entire MASCRAD team and my committee members for their vital support throughout the entire project, without the entire team this project would not have been a success. Lastly, I would like to acknowledge all of my past and current fellow graduate students Sanja, Ana, Nada, Elene, Aaron, and Pranav in the Electromagnetics lab for always being available to answer any questions I might have and for keeping the lab a fun environment to work in.

TABLE OF CONTENTS

LIST OF TABLES

LIST OF FIGURES

1. Introduction

In-situ measurements, remote sensing, and modeling of winter precipitation, which contains a large variability of ice particles, are being heavily investigated to better understand the microphysical characteristics of such particles [1, 2]. This paper focuses on in-situ measurements of hydrometeor shape, size, and composition using advanced optical instrumentation and methods, techniques of image and computational analysis, and processing of these measured characteristics to arrive at geometrical, physical, and scattering models of natural snow and ice particles. These models can further be processed and analyzed to compute realistic particle scattering matrices and full polarimetric radar measurables, namely, horizontal reflectivity, Z_h, differential reflectivity, Z_{dr}, linear depolarization ratio, LDR, specific differential phase, K_{dp}, and co-polar correlation coefficient, ρ_{hv}, to analyze microphysical characteristics of particles, perform studies of snow habits, and develop and use classifications of hydrometeor types.

The use of dual-polarized radar observables in conjunction with the microphysical properties of ice crystals and aggregates has been demonstrated as a useful and promising approach to classification of winter precipitation [3]. Conversion of these idealized microphysical characteristics of ice particles into a model that can be used to compute a scattering matrix and in turn radar observables poses great challenges due to the large amount of uncertainty in how accurately the proposed models represent winter precipitation. For instance, the scattering matrix is influenced by the winter particles density, a parameter that can vary substantially based on the type of particle as well as other factors, and when an incorrect density is used, large errors can be introduced [4, 5]. Furthermore, assuming idealized spheroidal shapes for ice particles instead of the more complicated realistic three-dimensional (3D) shapes can also

cause errors in the scattering matrix and in the determination of the snow water equivalent (SWE) [6, 7]. Some scattering models assuming spheroidal shapes for plate or column-like crystals have shown consistency with radar measurements [6, 8, 9, 10, 11, 12].

Kim showed that the use of spheroid approximations is only valid for smaller particles; as the snowflakes become electrically larger, the shape properties of the particles start to play a large role in scattering calculations [13]. Ishimoto performed the finite-difference time-domain scattering calculations of the backscattering cross-sections of ice particles using fractal based snowflake models [14]. These results showed large differences between equivalent-volume spheres and hexagonal columns, giving rise to the need for more accurate snowflake models. Furthermore, the evaluation of the sensitivity of snowfall characteristics at high frequencies, using idealized simulated snowflake models, indicated a need for a scattering database for large particles and aggregates as their shapes vary immensely and play a large role in determining snowfall characteristics [15]. Kim et al. created idealized ice crystal models in the form of hexagonal columns, four-arm rosettes, and six-arm rosettes, and used the discrete dipole approximation (DDA) method to calculate scattering effects of these geometries [16]. Multiple other papers present the use of the DDA method to compute single-scattering properties of synthetic randomly oriented idealized simple ice crystals. The results show that the scattering parameters of these idealized snowflakes are highly sensitive to shape and electrical size, again leading to the need for accurate and realistic models [16, 17, 18, 19, 20, 21]. Kuo et al. use the DDA method to compute the single-scattering properties of individual synthetic snowflakes, where each snowflake is simulated and averaged over 900 different directions [22]. These synthetic 3D snowflakes are created by a random aggregation, based on a sophisticated collection algorithm, of different pristine ice crystal models. The created synthetic 3D models

of aggregates have mass-versus-size and fractal properties that are consistent with field observations. A main conclusion of this work is that spherical particle models cannot be used to simulate single-scattering properties in a way that is consistent with the nonspherical snow particles of the same mass, across a very large frequency range, from 10 GHz to 183 GHz [22]. The discrepancies shown between complex snowflake models and spherical representations in this work give rise to the need for complex 3D models that accurately represent the snow that is falling at any given time.

However, even for Rayleigh scattering, while an assumption of spheroidal shape may provide reasonable results for the computation of reflectivity Z_e, it is not sufficient to accurately compute the full scattering matrix and the dual-polarization radar measurables such as Z_{dr}, LDR, and ρ_{hv} [23]. So even at the S-band (all WSR-88D radars), these radar measurables, which play an integral role in radar-based particle classification schemes, are highly shape dependent; this once more leads to the need for better and more realistic models of the winter precipitation particles.

Indeed, better and more realistic models of the winter precipitation particles can be obtained based on observations using advanced optical imaging disdrometers, which can record and measure actual geometrical shape, size, and composition properties of natural snowflakes and other hydrometeors in freefall. The 2D-video disdrometer (2DVD) measures fall speed along with projected hydrometeor views in two planes, namely, it gives two mutually orthogonal contour images of the particle, using high-speed line-scan cameras [24]. The multi-angle snowflake camera (MASC) captures high-resolution photographs of snow and ice particles in freefall from three views, while simultaneously measuring fall speed [25]. Teschl et al. used the 2DVD to create reconstructions of a snowflake based on two orthogonal views [26]. The two

orthogonal contours obtained from the 2DVD are intersected with a sphere that just encases the recorded particle, and parts of the sphere that do not intersect with the contours are deleted. Huang et al. use a similar method of creating reconstructions of particles imaged by a 2DVD by modeling the particle as an ellipsoid that just encloses the boundaries of the two orthogonal views obtained from the 2DVD [27]. Work by Garret et al. has involved creating a separate 3D reconstruction of a snowflake for each individual MASC image by extruding the 2D silhouette of the image until an equivalent volume, based off an equivalent radius determined from the image, is reached [25].

This paper proposes and presents a visual hull method and technique for reconstruction of realistic 3D shapes of snowflakes and other hydrometeors based on high-resolution photographs of particles in freefall from multiple views captured by a multi-angle snowflake camera. The visual hull of an object can be interpreted as the maximal domain that gives the same silhouettes as the object from a certain set of viewpoints. The 3D reconstructed snowflakes are represented by fine surface meshes of flat triangular patches, which capture a large amount of detail about the shape of the free-falling snowflakes. In order to improve the 3D reconstructions obtained from the visual hull method, two additional cameras are added to the three original cameras of the MASC, "externally," to provide additional 3D spatial information about the hydrometeor's shape. An improved mechanical calibration procedure of the MASC system involving all cameras of the system together is performed. Furthermore, a five-camera software self-calibration of the MASC is performed, to obtain a matrix describing the cameras internal and external parameters, which is then used as an input to the visual hull code to correct for a non-perfect mechanical calibration, a crucial step for the accuracy and reliability of shape reconstructions based on the MASC photographs. The fall speed measured by the MASC and the

horizontal cross-sectional projected area of the visual hull 3D reconstruction of the particle are used, along with state parameters measured at the MASC site, to estimate the particle mass, according to Böhm's method [28]. From the mass and volume of the meshed particle, an estimate the density is obtained, and then the dielectric constant for each snowflake, based on a Maxwell-Garnet formula. These scattering models of snow and ice particles can be used for computation of realistic particle scattering matrices and full dual-polarized radar observables; for instance, this can be done using a computational electromagnetics technique based on the higher order method of moments (MoM) in the surface integral equation (SIE) formulation [29]. To be able to perform scattering analysis by the MoM-SIE scattering code, the visual hull generated triangular mesh is converted to a mesh with curved generalized quadrilateral patches [29]. In addition, from these triangular patch meshes, representing realistic complex 3D shapes of snow and ice particles, the volume, surface area, shape characteristics, and spatial complexity of the hydrometeor are able to be computed, all extremely useful for various microphysical characterizations of winter precipitation.

Although this paper presents the methodology and technique for reconstruction of realistic 3D shapes of snowflakes and other hydrometeors based on MASC images, it can be adapted for use in conjunction with any other instrument providing high-resolution photographs of particles in freefall from multiple views. In addition, while the results in the paper are mostly for the snowflake shape reconstructions using five photographs of a hydrometeor collected by five cameras of the improved five-camera MASC system, the proposed technique can be applied to any number of photographs obtained by any number of cameras that provide sufficient spatial information about the object for the desired or sufficient accuracy of the reconstruction.

In addition to enabling realistic computation of "particle-by-particle" scattering matrices and polarimetric radar measurables for winter precipitation, the 3D shape reconstructions of hydrometeors by the proposed visual hull technique, in conjunction with the MASC or another similar instrument, can as well be used for studies of snow habits, for advanced analyses of microphysical characteristics of particles, and for hydrometeor classification. Finally, more accurate and realistic estimates of the particle volume, mass, and density, in conjunction with measurements of the particle size distribution (PSD), can significantly improve the radar-based estimation of liquid equivalent snow rates near the surface.

2. Multi-Angle Snowflake Camera, Modified MASC System, MASCRAD Instrumentation Site

The context of the proposed and presented visual hull method for reconstruction of 3D shapes of snowflakes and other hydrometeors is constituted by remote sensing observations and surface measurements, followed by analysis, of winter precipitation at an in-situ instrumentation site such as the newly built and established surface instrumentation field site for the MASCRAD (MASC + Radar) project [30, 31, 32, 33]. The MASCRAD Field Site, shown in Figure 1, at the Easton Valley View Airport, in La Salle, near Greeley, Colorado, includes a double wind fence housing a multi-angle snowflake camera (MASC), a two-dimensional video disdrometer (2DVD), a PLUVIO snow measuring gauge, a VAISALA weather station, and several other advanced instruments, such as a precipitation occurrence sensor system (POSS) and a meteorological particle spectrometer (MPS), as well as the collocated NCAR GPS advanced upper-air system sounding system trailer. These instruments operate under the umbrella of the state-of-the-art polarimetric weather radar, CSU-CHILL Radar, with the instrumentation site being very conveniently located at a range of 12.92 km from the radar.

At the heart of the MASCRAD project is the MASC, shown in Figure 2, which is a new instrument for capturing high-resolution photographs of snowflakes in freefall from three views, while simultaneously measuring their fall speed [25]. For Colorado State University's customized system, the horizontal resolution is 35 µm for all three cameras and the vertical resolution at 1-m/s fall speed is 40 µm, and the virtual measurement area is 30 cm^2. It has three identical cameras, 5 Megapixel (MP) Unibrain Fire-i 980b digital cameras, with identical lenses, Fujinon 12.5 mm. In a MASC, the angular separation in the horizontal plane between each of the two adjacent cameras is 36° and the camera-to-common focal center distance of 10 cm. Particles

that fall through the lower near-IR emitter-detector pair array simultaneously trigger each of the three cameras and the bank of LEDs. In addition to taking pictures, at a maximum triggering rate of 2 Hz, the fall speed of a particle is calculated from the time taken to traverse the distance between the upper and lower triggering arrays, which are separated vertically by 32 mm. In order to improve the 3D reconstruction obtained from the visual hull method, two additional lower-resolution cameras (1.2 MP Unibrain Fire-i 785b cameras, with 12.5-mm lenses) were added to the MASC, "externally" on an elevated plane with respect to the original three MASC cameras, as shown in Figure 2, to provide additional views – this will be discussed in detail later in the paper. Figure 3 shows three examples of MASC snowflake five-image sets collected at the MASCRAD Field Site.

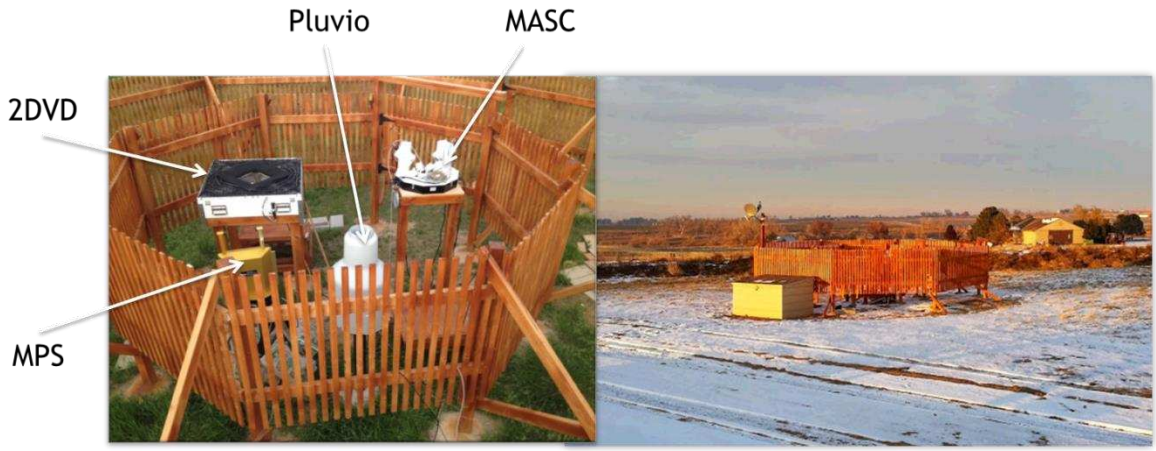

Figure 1. Field Site: MASCRAD Snow Field Site at Easton Valley View Airport, near Greeley, Colorado: 2/3-scaled double fence intercomparison reference (DFIR) wind shield housing various surface instrumentation; shown are MASC, 2DVD, Pluvio gauge, and MPS.

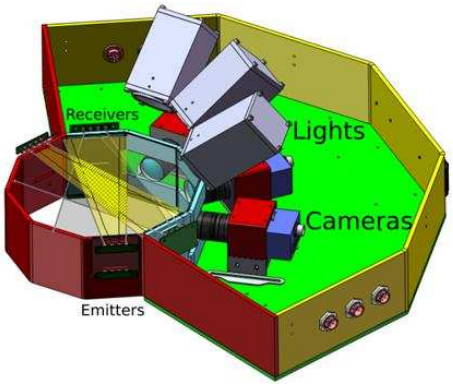

Figure 2. MASC: Multi-angle snowflake camera (MASC), with three cameras in horizontal plane for capturing high-resolution photographs of snowflakes in freefall and measuring their fall speed; CSU MASC system has two added "external" cameras (in temperature controlled enclosures) on an elevated plane, at about a 55° angle above horizon, to improve 3D reconstruction of snowflakes.

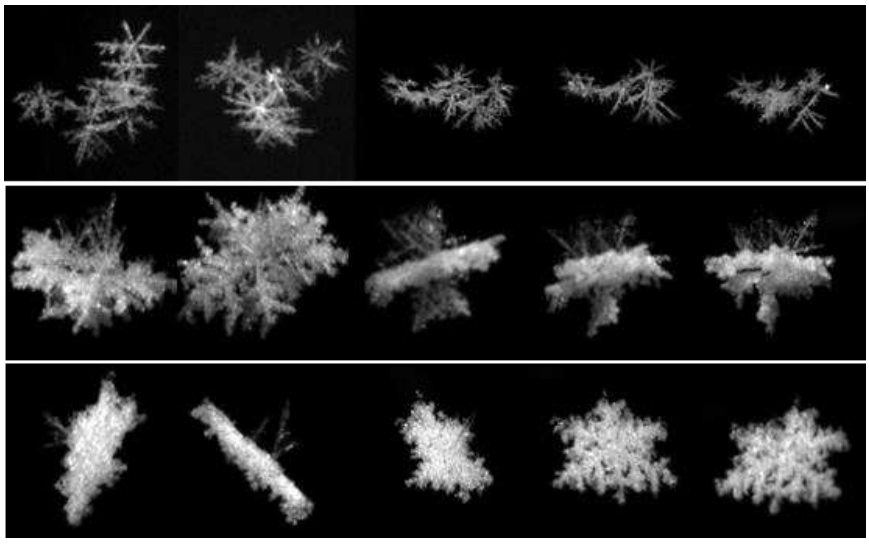

Figure 3. **Example Flake Images:** Three example sets, in three horizontal panels, of five photographs of three different snowflakes collected by five cameras of the new five-camera MASC system, in Figure 2, at the MASCRAD Field Site, in Figure 1. Each hydrometeor, in each horizontal panel, is imaged from five different views.

3. Visual Hull Method for 3D Shape Reconstruction of Snowflakes from Multiple Images

Proposed is the use of the visual hull geometrical method to reconstruct 3D shapes of hydrometeors based on the sets of five (or a different number) photographs obtained by the MASC (see Figure 1-Figure 3), or another similar instrument, and the corresponding 2D silhouettes of an object [34, 35]. This enables realistic computation of "particle-by-particle" scattering matrices, and can as well be used for studies of snow habits, for advanced analyses of microphysical characteristics of particles, and for particle classifications. The visual hull of an object can be interpreted as the maximal domain, or largest volume, that gives the same silhouettes as the object when viewed from a certain set of viewpoints (theoretically, from any viewpoint) [36]. The visual hull is obtained as an intersection of five visual solid cones formed by back-projecting, from the set of viewpoints, the previously found silhouettes in the corresponding image planes situated in front of the cameras, as illustrated in Figure 4. The visual cone of each silhouette refers to the projected volume of space extending from the camera's lens that the observed object lies completely inside. A limitation of the visual hull method is the inability to capture concave features due to these features not affecting the silhouette obtained from each image. This leads to the perfectly calibrated visual hull always being an overestimate of the object's volume as will be shown in the calibration section. In particular, an open-source MATLAB, C++ Visual Hull Mesh Code, which generates a visual-hull mesh from silhouette images and associated camera parameters, created initially for identifying stones based on certain shape parameters obtained from 3D reconstructions is used [37]. This code has been modified to work for the purpose of reconstructing snowflakes which are of a much smaller size scale.

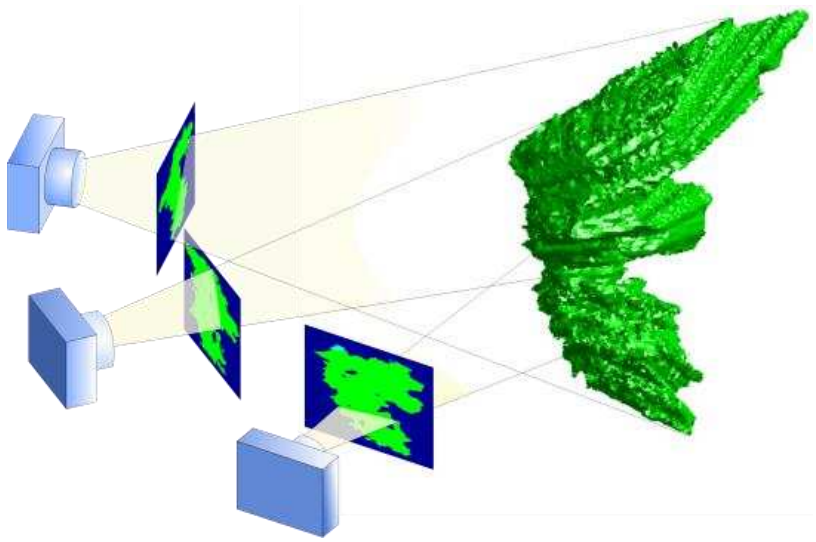

Figure 4. VH Method: Illustration of visual hull method with three cameras and their corresponding silhouettes projected and intersected with each other to obtain a 3D shape reconstruction of a hydrometeor.

The intersection of the visual solid cones creates a surface that reconstructs the hydrometeor's geometry. Each visual solid cone creates at least one closed surface region on the exterior of the hydrometeor's geometry; more than one surface region per visual cone is created if there are holes, or air gaps, present in the hydrometeor's silhouette. Points where the surface regions have a width of zero are called frontier points and are intersections of two or more visual solid cones. Frontier points lie directly on the actual hydrometeor's surface and regions near these frontier points are very accurately reconstructed. It is desired to have frontier points well distributed over a sphere in order to accurately reconstruct arbitrary shapes. As will be shown in a later section, the positions of the original three cameras in the MASC did not create representative reconstructions of snowflakes so two additional cameras were added (Figure 2) to aid in the even distribution of these frontier points.

Before the visual hull code can be run on a set of five (or three) images, a number of preprocessing steps must be taken to ensure quality 3D reconstructions. In order to determine what is part of the background and what is part of the foreground, a mean and standard deviation

of the background for all five (three) cameras is calculated over an hour period that corresponds to the image set being processed. The calculated mean and standard deviation are given as follows:

$$\overline{im} = \frac{1}{N}\sum_{i=1}^{N} im_i$$

$$STD\ (im) = \frac{1}{N-1}\sum_{i=1}^{N} (im_i - \overline{im})^2$$

where $\overline{im}$ is the mean, *STD* is the standard deviation, im_i is the matrix of the i^{th} image, and N is the number of pictures within the hour of calculation.

These calculated background values are used to subtract the backgrounds from the five images being processed to account for any variations in lighting conditions, changes in the background, the visible infrared bulbs, and all other variations that might occur from hour to hour and be mistaken as part of the foreground. Figure 5 shows an example of the mean and standard deviation calculated for use in background removal from MASC images. The IR bulbs used in sensing snowflakes can be seen by two of the five cameras (Figure 5, Cam3 and Cam 5) and appear as white dots in the image that visual hull will mistake for snowflakes. During daytime observations, the ground and DFIR fence slats (Figure 1) can be seen in the images. The background removal technique removes these bright spots, the fence slats, as well as other variations that might be mistaken for hydrometeors and allows for high quality reconstructions of snowflakes form the visual hull method.

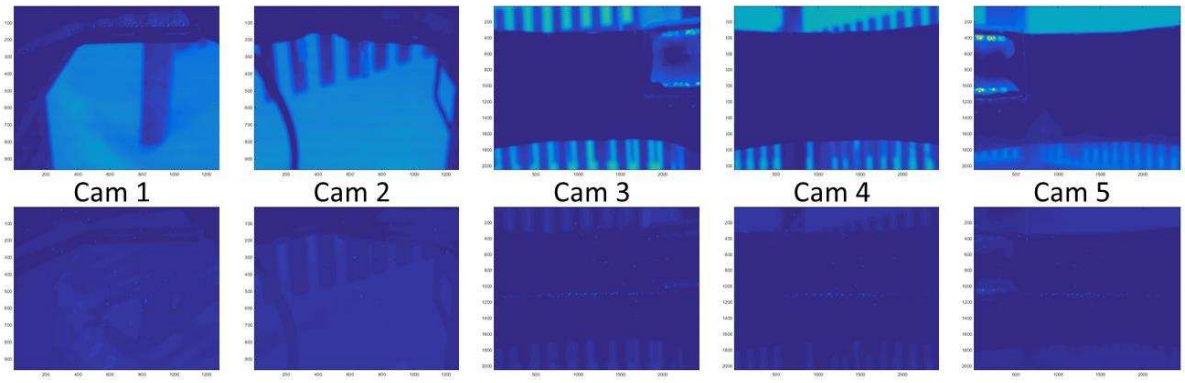

Figure 5. **Background Removal:** Mean (top) and standard deviation (bottom) of MASC background images for five cameras over one hour period on December 26th, 2014, hour 18 UTC. A total of 237 images were used in calculating the mean and standard deviation in this case.

The majority of the images collected by the MASC contain more than one snowflake per image, as shown in Figure 6. Before these images can be processed by the visual hull method, the snowflakes need to be counted, separated, and matched. If the images are input into visual hull without any pre-processing, the visual hull code will fail to create reconstructions for every snowflake. To do this, an image processing code has been created that boxes and counts the individual snowflakes present in each of the five images. Edge detection techniques are used to find where the snowflakes start and background ends and a box is placed around each individual snowflake, as depicted in Figure 7. Each camera's field of view (FOV) does not perfectly overlap, so the number of snowflakes imaged by each camera may be different. For the visual hull method to successfully create a 3D reconstruction, the snowflake must be present in each of the five camera's FOV. After the snowflakes have been boxed, the number in each image is counted and the image with the least number of snowflakes present is selected as the "starting image" for visual hull. In Figure 7, the image that contains the least number of snowflakes is seen by Camera 5 and contains 3 snowflakes and is called the starting image. This starting image is then dived into individual images where each image only contains one snowflake, while the other snowflakes are blacked out and removed (Figure 8). Each of these separated individual

snowflakes, three in this example, are run through visual hull with the remaining four images. If these three snowflakes are present in the FOV of the other 4 cameras, a 3D reconstruction will be created for each of them.

Figure 6. Multiple Flake Images: Examples of multiple-snowflake images recorded by the MASC from varying snow events, on December 26th, 2014 (left panel), February 16th, 2015 (central panel), and March 3rd, 2015 (right panel), respectively.

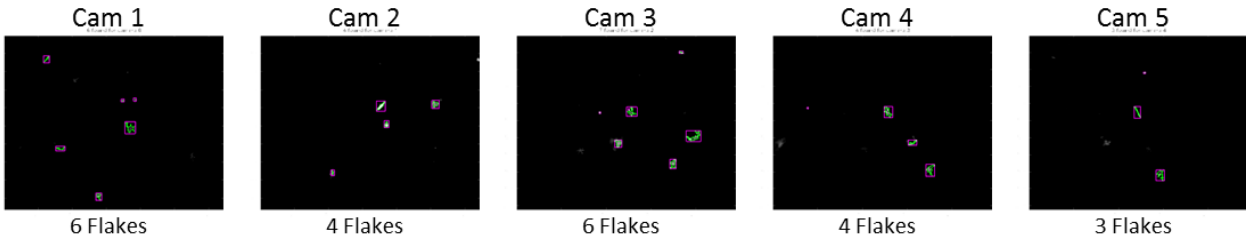

Figure 7. Boxing and Counting: Set of MASC images with snowflakes boxed and corresponding number observed in each image. Camera that contains the least number of snowflakes is used as starting image for visual hull, Cam 5 in this example. The snowflakes were observed on March 3rd, 2015.

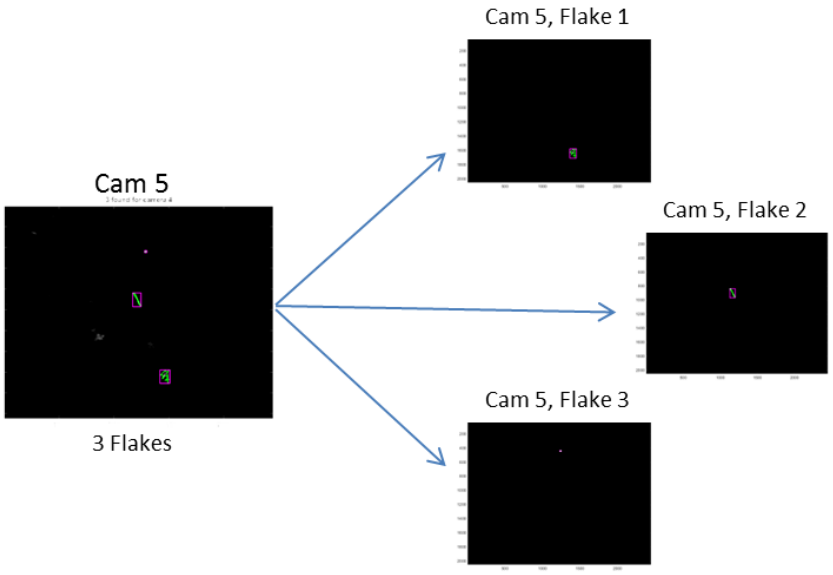

Figure 8. Starting Image: Camera 5 from Figure 7 split into 3 individual images with only one snowflake per image.

Along with the five images input to the visual hull code, many parameters that define the camera properties and positions must also be defined and input to the code. These parameters include the camera rotation and translation in 3D space, called the extrinsic parameters, and the focal point, principal points, and distortion, called the intrinsic parameters. A self-calibration code described in the following section gives a way to accurately compute these extrinsic and intrinsic parameters. Other parameters given as inputs to the visual hull code include the resolution of each camera and the size of each camera's charge-coupled device (CCD). For the CSU MASC (Figure 2), the original three "internal" cameras have a 5 MP resolution, 2448 x 2048 pixels, a 12.5 mm focal point, a 2/3" CCD sensor, and a working distance (to the point at which the cameras are focused) of 10 cm. The additional two "external" cameras have a 1.2 MP resolution, 1288 x 964 pixels, a 12.5 mm focal point, a 1/3" CCD sensor, and a working distance of 16 cm.

After background removal process, multiple-snowflake image preprocessing, and specification and input of all camera parameters, the working volume, i.e., the volume

intersection of all five camera's FOVs, is discretized into voxels of a desired size to adequately represent the hydrometeor's geometry. The five images are transformed into silhouettes made up of polygons of a desired size. The visual hull code then randomly searches for a center point of a voxel that can be projected to each of the five camera's silhouettes that represents the snowflake within each of the images. Once a point is found, the code starts to build a voxel grid around the projected point until no more voxel center points can be projected to all five cameras. These voxels are then polygonised into a triangular surface mesh using the method developed by J. Bloomenthal [38]. After the 3D surface reconstruction of the hydrometeor is generated, it is re-projected onto the 2D images as green silhouettes to check how well the geometry matches and represents the 2D images. An example of the 3D reconstruction from a set of five MASC photographs and the 2D re-projection of the reconstructed shape onto the original five images is shown in Figure 9. The size of the voxel grid and triangular mesh patch can be set to capture the desired amount of details and fine features, as depicted in Figure 10.

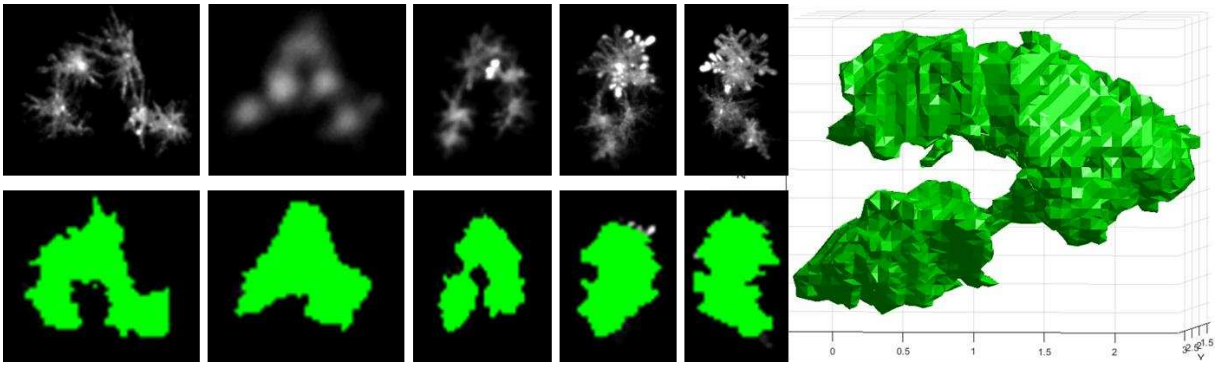

Figure 9. **3D Reconstruction Example:** Example of the visual hull 3D reconstruction of a snowflake (right) based on five MASC images (top left); the corresponding 2D re-projections of the 3D reconstructed shape onto images are also shown (bottom left).

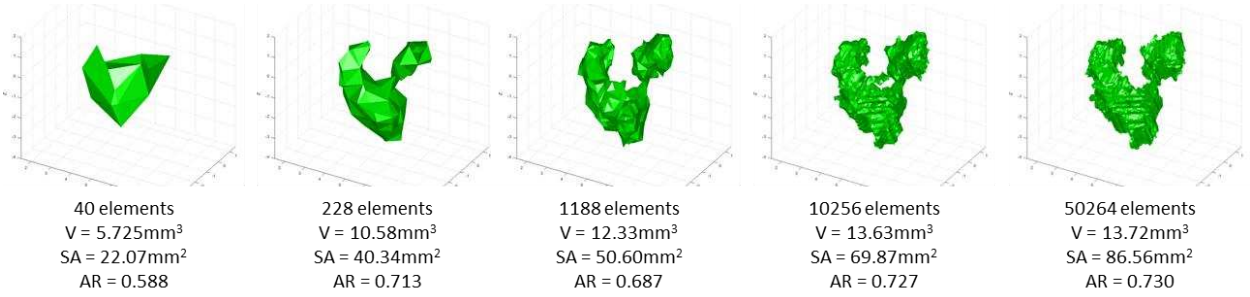

Figure 10. Mesh Refinement: Visual hull 3D reconstructions of the same snowflake shown in Figure 9 using several decreasing voxel sizes. Number of triangular elements, volume (V), surface area (SA), and aspect ratio (AR) are given for each reconstruction.

As can be seen in Figure 10, changing the voxel size in visual hull changes the volume, surface area, shape and aspect ratio of the snowflake. Decreasing the voxel size leads to a more accurate representation of the snowflake at the expense of more computational time. To determine what voxel size should be used, a random set of snowflakes was reconstructed multiple times with a decreasing voxel size. The percent change after each refinement of the reconstruction's volume and surface area are plotted in Figure 11. The level of refinement number corresponds to the number of divisions along one side of a box that bounds the working volume of the five cameras. After a level of refinement of 500, the change in volume, surface area, and aspect ratio is less than 5%, and for this reason a level of refinement of 500 is adopted as a general parameter in the method for all further reconstructions.

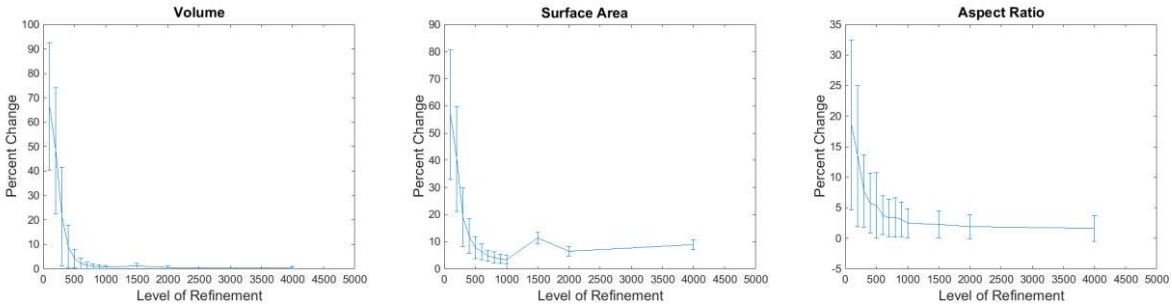

Figure 11. Convergence of Mesh Refinement: Convergence of volume (left panel), surface area (central panel), and aspect ratio (right panel) of a random set of 150 snowflake reconstructions with a decreasing voxel size (increasing level of refinement).

The final 3D model is represented by a mesh of flat triangular patches. These triangular patch meshes, representing realistic complex 3D shapes of snow and ice particles, are used for scattering computations by means of the method of moments computational electromagnetics code, to obtain "particle-by-particle" scattering matrices and polarimetric radar observables. In addition, from these meshes, the volume, surface area, shape characteristics, and spatial complexity of the hydrometeor are able to be computed, all extremely useful for various microphysical characterizations of winter precipitation.

As shown in Figure 2, the original MASC is a 3 camera system where all of the cameras are coplanar and separated by 36° with respect to each other in the azimuthal direction, covering only 72° in front of the object. The visual hull method works best when cameras are well distributed over a sphere and focused at the sphere's center [39]. When looking at a large number of reconstructions generated when only using three coplanar cameras, the 3D reconstructed snowflakes from the three MASC photographs are, generally, not close enough to the real shapes of the hydrometeors. For this reason, two additional cameras were added to the MASC externally on an elevated plane, 55° with respect to the horizon and 72° away from the outer original cameras. The positions of these additional cameras were chosen based on two main requirements: obtaining the most new information, i.e., new azimuthal angles and a different elevation plane; and the mechanical constraints of placing the cameras keeping in mind where the light sources are. Table 1 gives the azimuthal and elevation positions of all five cameras in the new MASC system.

Table 1. Camera Positions: Azimuthal and elevation angles of all five cameras in the new MASC system, in Figure 2.

	Azimuth [degrees]	Elevation [degrees]
Camera 1 (original)	0	0
Camera 2 (original)	36	0
Camera 3 (original)	72	0
Camera 4 (addition)	144	55
Camera 5 (addition)	288	55

4. Mechanical Calibration and Software Self-Calibration of the Five-Camera MASC System

The visual hull 3D reconstruction method assumes that the camera system is perfectly calibrated, meaning that the intrinsic and extrinsic parameters of the system are perfectly known. The extrinsic parameters refer to the rotation matrix, R^i and translation matrix, t^i for each of the five camera positions, and to the positions and orientations of the five cameras in physical space. The intrinsic parameters of the cameras refer to the focal length, principal points, and distortion, and are dependent on the camera body and the camera lens.

These extrinsic and intrinsic parameters were initially estimated and input into the visual hull code. The estimation of the extrinsic parameters was based on the theoretical camera positions as determined by the manufacturer of the device. The intrinsic parameters were estimated using theoretical equations that relate them to the camera and lens parameters as follows:

$$M_{res} = \frac{FOV}{R}, \qquad M_{res} = \frac{P_s * FOV}{S_s}, \qquad R = \frac{d_f}{P_s}$$

$$FOV = 2 * d_s * \tan\left(\frac{AOV}{2}\right), \qquad AOV = 2 * \arctan(\frac{d_f}{2 * f})$$

$$R = \frac{1000 * 10^{-6}}{2 * P_p}, \qquad d_f = P_p * R$$

with description of variables given in Table 2.

Table 2. Camera Parameters: Description of variables used in intrinsic camera parameter equations, resulting in estimates for a starting point in the self-calibration software.

M_{res}	$Micron\ Resolution$

R	$Resolution\ (number\ of\ pixels\ 1D)$
FOV	$Field\ of\ View$
AOV	$Angle\ of\ View$
P_s	$Pixel\ Size\ (parameter\ of\ CCD)$
d_s	$Distance\ to\ Subject\ (working\ distance)$
d_f	$Sensor\ Size(1D)$
f	$Effective\ Focal\ Length$
P_p	$Pixel\ Pitch$
DOF	$Depth\ of\ Field$

These estimations may be acceptable for 3D reconstructions of larger objects such as fruits or people; however, for the size scale of snowflakes, every pixel counts and they are not sufficient. The 3D reconstructions of snowflakes created using estimated intrinsic and extrinsic parameters are not representative of the actual snowflakes geometry. Reconstructions are rarely able to be created when these estimation of camera parameters are used. When projecting the 3D reconstruction, if it is able to be created, as silhouettes onto the original image set, the coverage of the re-projection is very poor and much of the snowflakes geometry is cut off and ignored. To fix these mismatches and poor reconstructions, mechanical and software calibrations of the camera system were implemented.

The mechanical calibration procedure involves positioning the five cameras in such a way that they are focused on a single point as close as possible. To do this, instead of a standard procedure of using a target grid that is moved between all of the five cameras separately, one calibration grid is placed in the center of the observational area at a 30° angle so that it is completely visible to all five cameras simultaneously. A 5 x 5 calibration grid, with crosshairs in the center grid, created with known black and white box sizes of 5 mm, is used as the calibration target. The cameras are then individually run in a video mode so their image can be seen in real time on a computer screen. Using MB-Ruler, a reference grid is overlaid on the computer screen with crosshairs at the center of the screen [40]. For each camera, the camera mount is

mechanically adjusted, as precisely as possible, to overlap the physical crosshairs on the calibration grid with the crosshairs on the computer screen, as shown in Figure 12. The focal point of the camera is then adjusted to be as close to the center of the crosshairs as possible. The mechanical calibration allows for the depth of field (DOF) of all cameras to overlap as much as possible, which leads to a greater number of image sets where all 5 images are in good focus. Another parameter that is experimentally calculated based on the grid used in the mechanical calibration is the horizontal and vertical field of view (FOV) of the cameras. After mechanical calibration is complete, a new test to characterize the DOF and its relationship with the size of the particle was implemented based on previous work related to the snowflake video imager (SVI) [41]. The DOF along with the FOV are very important parameters used to calculate the observed volume, which is needed when calculating the particle size distribution of snowflakes from the individual cameras.

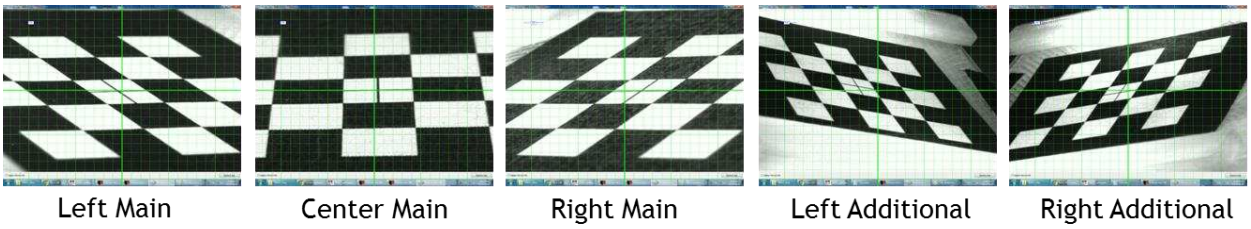

Figure 12. Calibration Grids: Calibration grid used in the mechanical calibration for the five cameras (three main, original "internal", MASC cameras and two additional, "external", cameras, Figure 2): matching of the physical calibration grid in camera's working volume with the grid on computer screen.

However, even with this mechanical calibration procedure implemented, the visual hull reconstructions still miss parts of the snowflakes geometry, as shown in Figure 13. A software calibration was implemented to adjust for this imperfect mechanical calibration. Namely, an open source multi-camera software self-calibration is utilized with modifications to accurately estimate the internal and external parameters of each camera, which, in turn, are used to calculate

the position matrix, needed as an input for visual hull [42]. The main functionality and implementation of the self-calibration algorithm is laid out below.

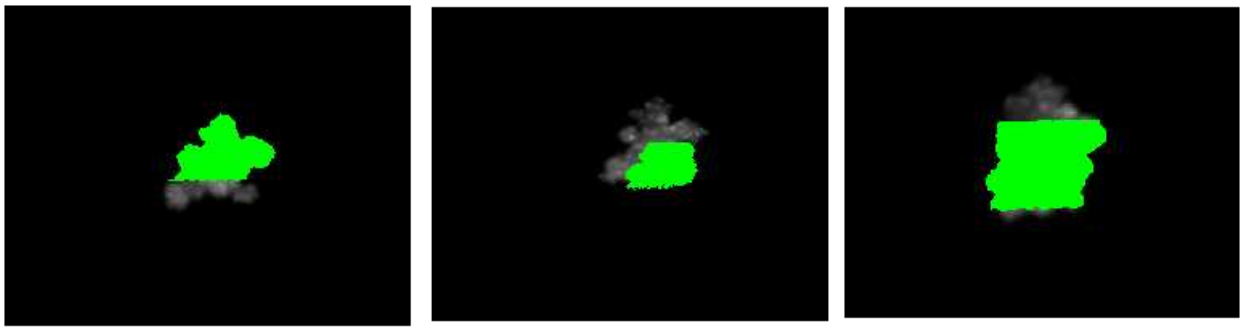

Figure 13. Re-projection Errors: 2D re-projections (green areas) of the 3D reconstruction of a snowflake over the images (gray areas) from the three original MASC cameras. Coverage of projections is poor due to an imperfect calibration of the camera system.

The input to the self-calibration code is a collection of "point images" that adequately fill up the working volume of the cameras, i.e., the volume that is visualized by all five cameras simultaneously. A thin bamboo stick that is painted black with a small white tip is moved around the working volume while the cameras are manually triggered. The projections of these points in each of the 2D images are initially detected by first computing the mean and standard deviation of the background and comparing the actual image to these computed background images. If the detected point is much larger than expected, if the pixels of the detected point are not connected, or if the detected point contains motion blur based on the eccentricity of the point, the image is discarded and is considered a mis-detected point. The detected points are resampled to obtain higher resolution and then a 2D Gaussian function is fit to the point to determine its position. Constraints based on epipolar geometry, in the form of geometric relations between 3D points and their 2D projections based on 2 cameras, further remove any mis-detected points. A random sample consensus (RANSAC) method is used to iteratively determine epipolar geometry of camera pairs and removes any points that do not fit within the epipolar constraints of the cameras. A scaled measurement matrix W_s is constructed as

$$W_s = \lambda_j^i \begin{bmatrix} u_j^i \\ v_j^i \\ 1 \end{bmatrix} = \lambda_j^i \boldsymbol{u_j^i} = P^i \boldsymbol{X}_j$$

where $\boldsymbol{X}_j$ corresponds to the 3D coordinates of the j detected points, $\boldsymbol{u_j^i}$ are the pixel u-v coordinates, u_j^i and v_j^i, of the 2D projected j points for camera i, λ_j^i is the projective depth for the j^{th} point on the i^{th} camera, and P^i is the projection matrix for the i^{th} camera that contains the cameras position, internal parameters, and external parameters [42]. The variables being estimated in the self-calibration code are the projective depths λ_j^i and the projection matrices P^i. Initially it is assumed that $\lambda = 1$ and then an estimate of the projective depth is obtained from the images iteratively according to the method of Sturm and Triggs to obtain the optimized W_s, and in turn the projection matrices P^i **[**43**]**. Once the projection matrices are known they can be decomposed into an internal and external parameter matrix, and a position matrix that is needed as an input to the visual hull code.

This corrected position matrix is input into the visual hull code and is used to correct for the non-perfect mechanical calibration. After both mechanical and software self-calibration have been implemented, the projections of the 3D reconstructed geometries as silhouettes onto the original snowflake images show over 90% coverage in all cases, as can be seen in the results section.

Another method to obtain the images needed for the software calibration code is being developed based on a similar calibration grid that is used for mechanical calibration, the only difference being the grid size is increased to 8 x 8 to facilitate the ease of obtaining multiple points. The calibration grid is moved around the measurement volume of the cameras while the cameras are manually triggered. The code is being modified to accept the grids instead of point images, and now treats each white square on the grid as the point images. A large enough set of

images is easily obtained due to the large number of white squares on the grid, and these images are input into the software calibration code. Once completed, this method will be much faster and will require much fewer input images, with 64 points per image, as compared to the method using the bamboo stick, which only contains one point per image and so requires a large number of images.

5. Meshing, Dielectric Constant Estimation, Scattering Analysis, and Automatization of Process

Our scattering models of snow and ice particles and computation of realistic particle scattering matrices and full polarimetric variables are based primarily on the higher order method of moments (MoM) in the surface integral equation (SIE) formulation [29, 44, 45]. In this technique, the surface of a dielectric scatterer (precipitation particle) is modeled using generalized curved quadrilateral patches, with unknown electric and magnetic equivalent surface currents over the patches being approximated by means of known polynomial basis functions with unknown current-distribution coefficients. These coefficients are determined by solving surface integral equations (SIEs) based on boundary conditions for electric and magnetic fields on the surface of the particle, employing the Galerkin method.

Since our MoM-SIE scattering code uses curvilinear quadrilateral meshes of particles, and the final output of the visual hull 3D reconstruction code is a mesh of flat triangular patches, a method based on ANSYS ICEM CFD meshing software has been created to convert the VHMC-generated mesh to a mesh with curved generalized quadrilateral patches [46]. Due to the number of snowflakes that need to be meshed, the ability to automate the meshing process was a necessity. ANSYS has the ability to be controlled via TCL scripts and batch files. This feature was utilized and TCL scripts were written to perform the multiple meshing steps within ANSYS all the way from file import to exporting a good quality mesh. The script file automates the multiple step process of obtaining a good quadrilateral mesh with no user input. First the STL (stereolithography) file obtained from the visual hull code is imported as a solid geometry instead of a triangular mesh. Then the geometry is checked for errors and a watertight volume is created. The size of the snowflake is analyzed and meshing parameters are specified based on

this size to create a mesh with the desired number of elements to adequately represent features of the geometry. A maximum element count can be set, and if the mesh exceeds this limit the snowflake is re-meshed using larger elements. The TCL script file was written to take as an input a folder containing multiple STL files and convert them to quadrilateral meshes with no user input. The script utilizes many of the built in mesh quality checks and auto repair features that ANSYS contains in order to correct any misshaped or poor quality elements. The mesh is checked for intersecting elements, negative determinants, size uniformity, and angles of connecting elements, as well as other parameters needed for a good quality mesh. Note that such mesh checks and improvements would be needed even if a scattering code based on a mesh of flat triangular patches as input were used.

Figure 14 shows examples of 3D shape reconstruction of real snow particles using the VHMC code and ANSYS ICEM CFD meshing software. The script then extracts and saves node and element data that is needed for the MoM-SIE input file. These node and element files are passed to a MATLAB code that automatically reorders and formats the data to match the MoM-SIE input file. The MATLAB code then creates a folder containing all of the MoM-SIE input files that are run via a batch file.

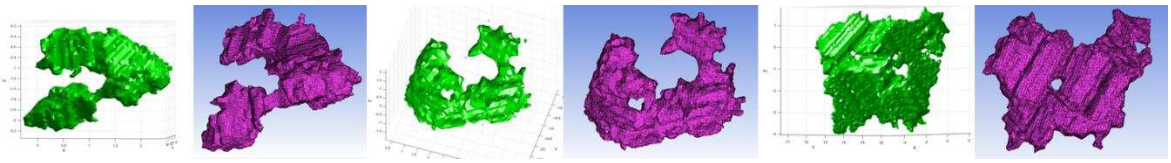

Figure 14. VH and ANSYS Meshes: Visual hull 3D reconstructions of hydrometeors, shown in green, represented using triangular patches and the corresponding conversion of the reconstructions to quadrilateral meshes, shown in purple, using ANSYS meshing software.

In addition to the realistic representation of the 3D shape of a hydrometeor, an estimate of its dielectric constant is needed, to be able to perform scattering computations using the MoM-SIE code. From the triangular patch meshes (e.g., in Figure 9), the volume of the 3D

reconstructed particle is able to be computed, within the visual hull code, thus obtaining the volume estimation for the hydrometeor, which is needed for the estimation of the dielectric constant. Furthermore, the horizontal cross sectional drag information is obtained from the 3D particle reconstruction, i.e., the particle's projected area presented to the flow, that is used in Böhm's method, in conjunction with the recorded fall-speed of the particle and environmental conditions such as air density, viscosity, and temperature measured at the MASC site, to estimate the particle's mass [28]. This is done similarly to the approach described in Huang et al. [27]. From the mass and volume, the effective density or porosity of the particle (snowflake) is determined, from which, in turn, its effective dielectric constant, ε_r, is obtained based on a Maxwell-Garnet formula. Such ε_r takes into account air inclusions and partly melted regions of ice crystals, apart from some of the porosity of the ice particle captured by the MASC/visual hull, along with its complex shape.

Scattering analysis of the 3D reconstructed snowflakes, with the estimated dielectric constants, is performed on a particle-by-particle basis by means of the MoM-SIE method and is used to compute polarimetric radar measurables (Z_h, Z_{dr}, LDR, K_{dp}, and ρ_{hv}), which are then analyzed and compared against the corresponding data collected by the CSU-CHILL radar.

Due to the large quantity of data collected, e.g., approximately 500,000 snowflakes captured and recorded at the MASCRAD Field Site (shown in Figure 1) during the 2014/2015 winter season, the data processing must be completely automatic from the collection of the image sets to the generation of the radar observables. To do this, a MATLAB control code was created that connects and automates all of the individual processes. The only user input is determining which snowflakes to process, in terms of snowflake IDs, a parameter defined during MASC image capture, or a time range. Once the range is specified, the image processing code that boxes,

counts, and separates snowflakes is run. The output of this code is used as an input to the visual hull code and triangular patch meshes are generated for all possible cases. These meshes are used in conjunction with the TCL script as an input to ANSYS meshing software, which performs re-meshing as described above and outputs the corresponding quadrilateral patch meshes. The quadrilateral meshes are then converted into a suitable format that can be input into the MoM-SIE scattering code, which, in turn, computes and outputs "particle-by-particle" scattering matrices. The final step is a conversion of these matrices into the polarimetric radar observables. The automatic process is outlined in Figure 15 below.

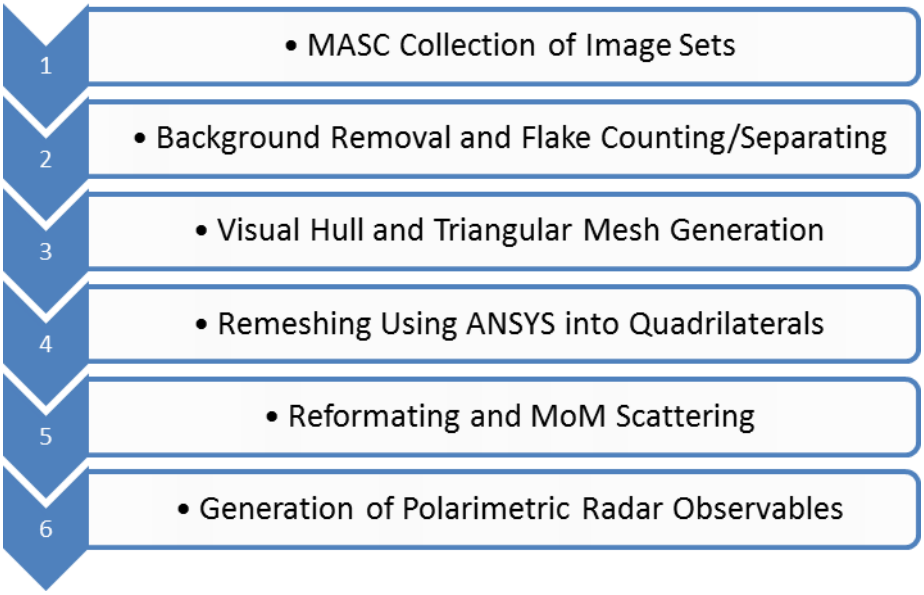

Figure 15. Automatic Control Process Flow: Outline of steps of the automatic MASC/visual-hull/meshing/scattering observation/analysis process for each collected and analyzed snowflake starting from collection of data to computation of radar observables.

6. Results and Discussion

First, to test the accuracy of 3D reconstructions based on three cameras (three main, original "internal", MASC cameras) vs. five cameras (with two additional, "external", cameras) in Figure 2, simulated images of a sphere with a 3 mm diameter were generated and input into the visual hull code. The sphere was assumed to lie at the exact center of all cameras focal point. At this point, the micron resolution of the cameras, the size of each pixel in the image in micrometers, is 35.9 μm for the 5 MP cameras and 89.6 μm for the 1.2 MP cameras. This leads to the simulated 3 mm diameter sphere 2D image to have a diameter of approximately 83.5 pixels and 33.5 pixels in the 5 MP, and 1.2 MP cameras, respectively. The volume, surface area, aspect ratio, and parameters relating to the deviation of the 3D points, nodes, of the reconstructed sphere were compared to the theoretical value. The results are shown in Table 3.

Table 3. Sphere Reconstruction Comparison: Comparison of sphere reconstruction based on the original three-camera MASC and the new five-camera MASC (Figure 2).

	3 Camera	5 Camera
Volume [% Error]	27.03	5.31
Surface Area [% Error]	27.35	6.43
Aspect Ratio	0.5974	0.8569
Average Deviation of Nodes from Surface [% Error]	12.45	2.54
Maximum Deviation of Nodes from Surface [% Error]	66.79	26.98
Standard Deviation of Nodes [mm]	0.25	0.064
Percent Nodes < 10% Error from Surface	65.19	92.91
Percent Nodes < 5% Error from Surface	56.10	85.37
Percent Nodes < 1% Error from Surface	26.10	51.72

As can be observed from Table 3, the five-camera MASC outperforms the three-camera MASC drastically with lower percent error in every category as well as having an aspect ratio

much closer to one. In both cases, the volume and surface area of the reconstructed sphere are overestimates of the actual values. The deviation from surface parameter gives a value relating to how far a node on the reconstructed geometry is from the actual theoretical sphere. A deviation from surface value of 0% indicates the reconstructed node lies exactly on the theoretical sphere's surface. The camera positions and 3D views of the corresponding sphere reconstructions for the three- and five-camera MASC systems are shown in Figure 16 and Figure 17, respectively. The five-camera reconstruction more closely represents a sphere from the different angles as opposed to the three-camera version, which shows a diamond like shape in some views.

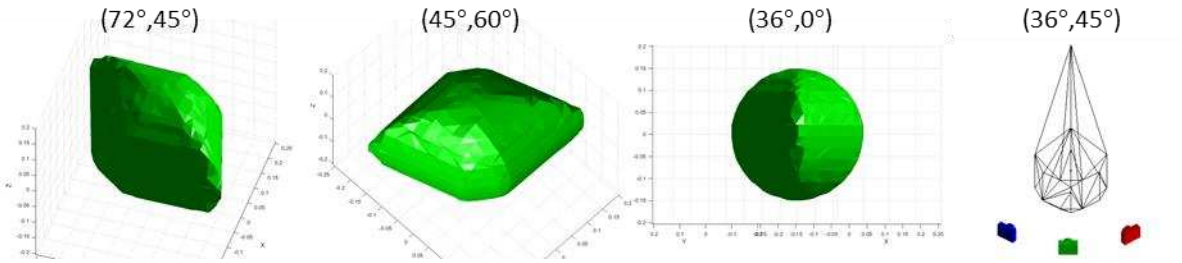

Figure 16. 3 Camera Sphere Reconstruction: (three left panels) Three-camera sphere reconstruction viewed from three different spatial directions defined by (azimuth angle, elevation angle). (right-most panel) Spatial positions of the three cameras and their FOV intersection, i.e., measurement volume.

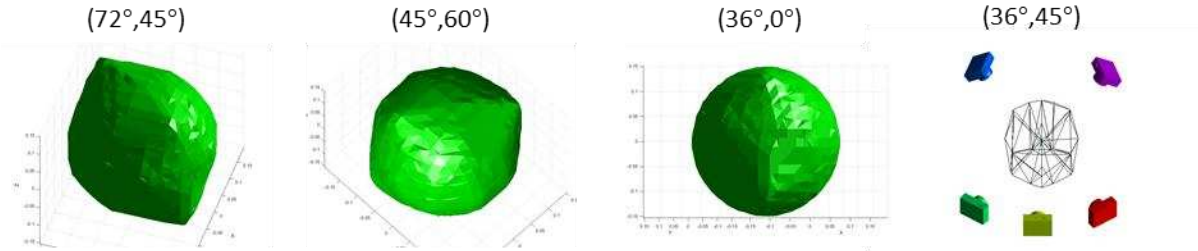

Figure 17. 5 Camera Sphere Reconstruction: The same as in Fig. 16 but for five-camera sphere reconstruction.

In order to further demonstrate and evaluate the improvement achieved by adding the two upper cameras, Figure 18 shows 3D visual hull reconstructions of several snowflakes of complex shapes, captured at the MASCRAD Field Site (Figure 1), based on photographs from three and five MASC cameras, respectively, along with the computed volume, surface area, and aspect

ratio values. As can be observed from the figure, the reconstructions based on five cameras all have smaller volume and surface area than the corresponding three-camera reconstructions. In some cases, as can be seen in Figure 18, the addition of the two cameras drastically changes the reconstructed shape.

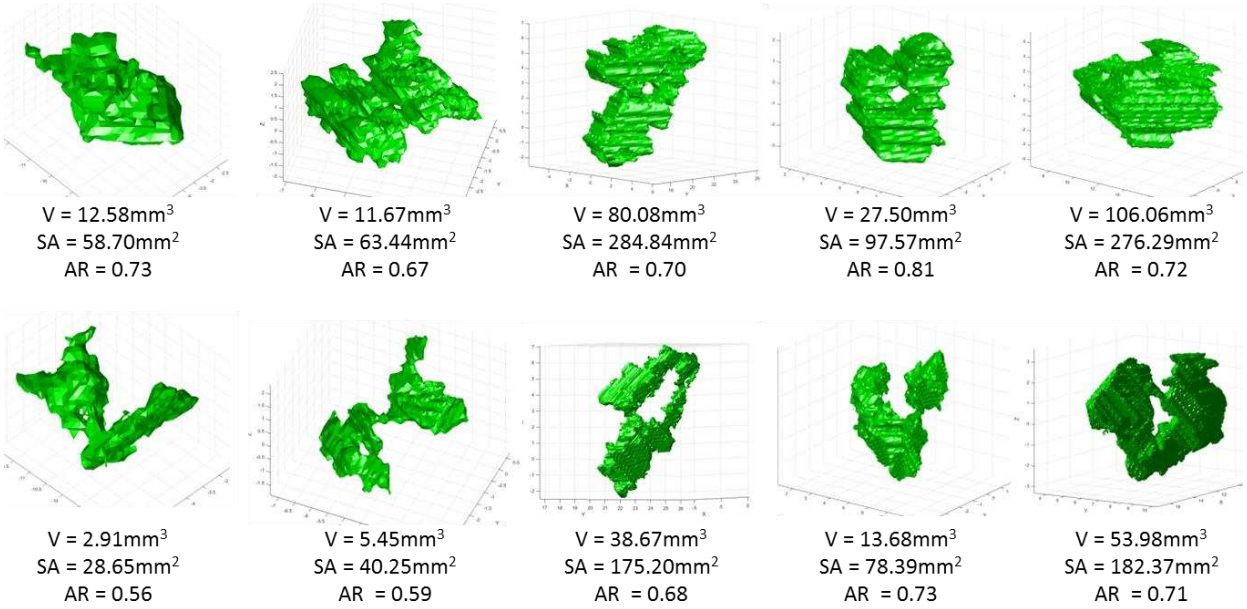

Figure 18. 3 Camera versus 5 Camera reconstructions: 3D reconstructions of five different recorded snowflakes based on three-camera (top panels) and five-camera (bottom panels) MASC instruments. For each reconstruction, the corresponding computed volume (V), surface area (SA), and aspect ratio (AR) are given as well.

Next, to show how well the visual hull method can reconstruct complicated snowflake-like shapes in cases where the actual shapes of the objects are known, fake snowflakes that were 3D printed were dropped through the five-camera MASC. These fake snowflakes were created using 3D CAD modeling, so they have known volumes and surface areas. The images of these objects obtained by the MASC were run through the visual hull code and 3D reconstructions were generated. Sources of error in this method and measurement include the resolution of the 3D printer, and the unknown volume and surface errors of the 3D printed snowflakes. Another source is dependent upon at what angle the fake snowflake falls through the MASC and how well it is resolved in each image. Namely, the volume and surface area of the 3D reconstructed

snowflake will somewhat vary depending on the entrance angle of the object as it is dropped through the MASC. The reconstructed shapes, their corresponding MASC images, the 2D projections of the 3D reconstructions, as well as comparisons between the volume, surface area, and aspect ratio of the reconstructions and the respective values of the 3D CAD models of 3D printed snowflakes, are shown in Figure 19, where very good results of the visual hull shape reconstruction can be observed in all cases. For reference, Figure 19 also gives the percent error with respect to the CAD models for the volume if the fake snowflakes are reconstructed using a spheroid approximation in place of the visual hull method.

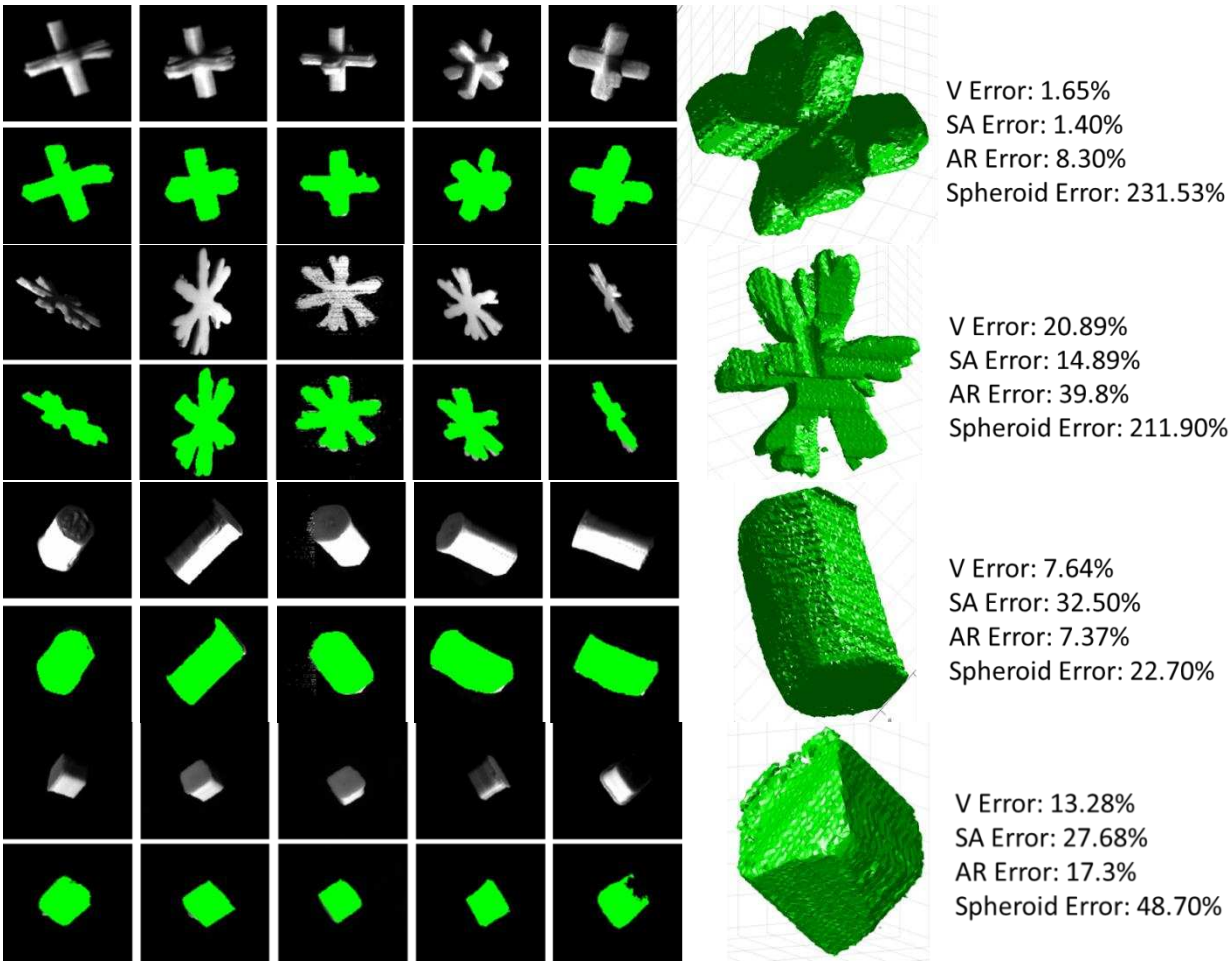

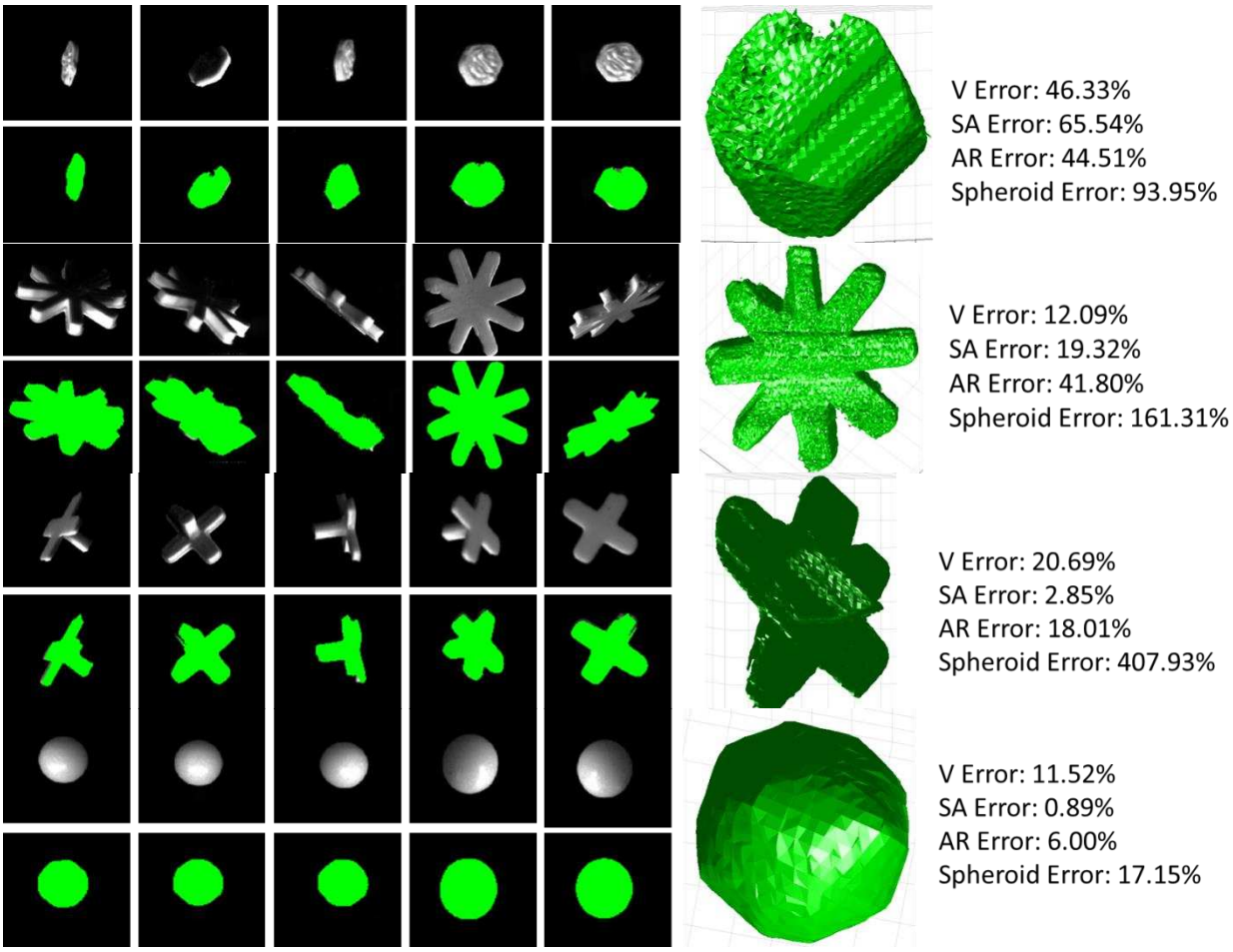

Figure 19. 3D Printed Flakes VH reconstruction: Visual hull reconstructions of 3D printed fake snowflakes and the corresponding MASC images, along with the projections of 3D reconstructed shapes onto 2D images. Percent errors of the volume (V), surface area (SA), and aspect ratio (AR) of the 3D reconstructions relative to the V, SA, and AR values of the 3D CAD models of 3D printed snowflakes are given as well. The volume percent error with respect to the V of the CAD models is shown also for the reconstructions of fake snowflakes using spheroids instead of the visual hull method.

Further, Figure 20 shows 20 examples of 3D reconstructions of different snowflakes collected at the MASC site, near Greeley, Colorado, during a snow event that occurred on February 23rd, 2015. For each snowflake, the five images (photographs) obtained by the modified MASC system are shown along with the 3D reconstructed shape triangular mesh obtained by the visual hull method and its back projections onto the original images, as well as the information about the volume, surface area, and aspect ratio of the reconstructed snowflake. Observed from the results, is an ability of the presented visual hull method to successfully and accurately

perform 3D reconstruction for snowflakes of very realistic, complicated, and diverse shapes and compositions, and very different sizes and complexities, which in addition to demonstrating the power of the visual hull approach, confirms – in experiments involved in a real snow storm observation – availability of sufficient silhouette information from the five cameras of the modified MASC system for 3D reconstruction and excellent mechanical and software self-calibration of the system. Also observed is an almost perfect re-projection of the 3D reconstruction of every snowflake and excellent coverage of the projections of the 3D reconstructed geometries as silhouettes onto the original snowflake images (the green areas practically perfectly cover the gray areas for all snowflakes and all five images for each snowflake).

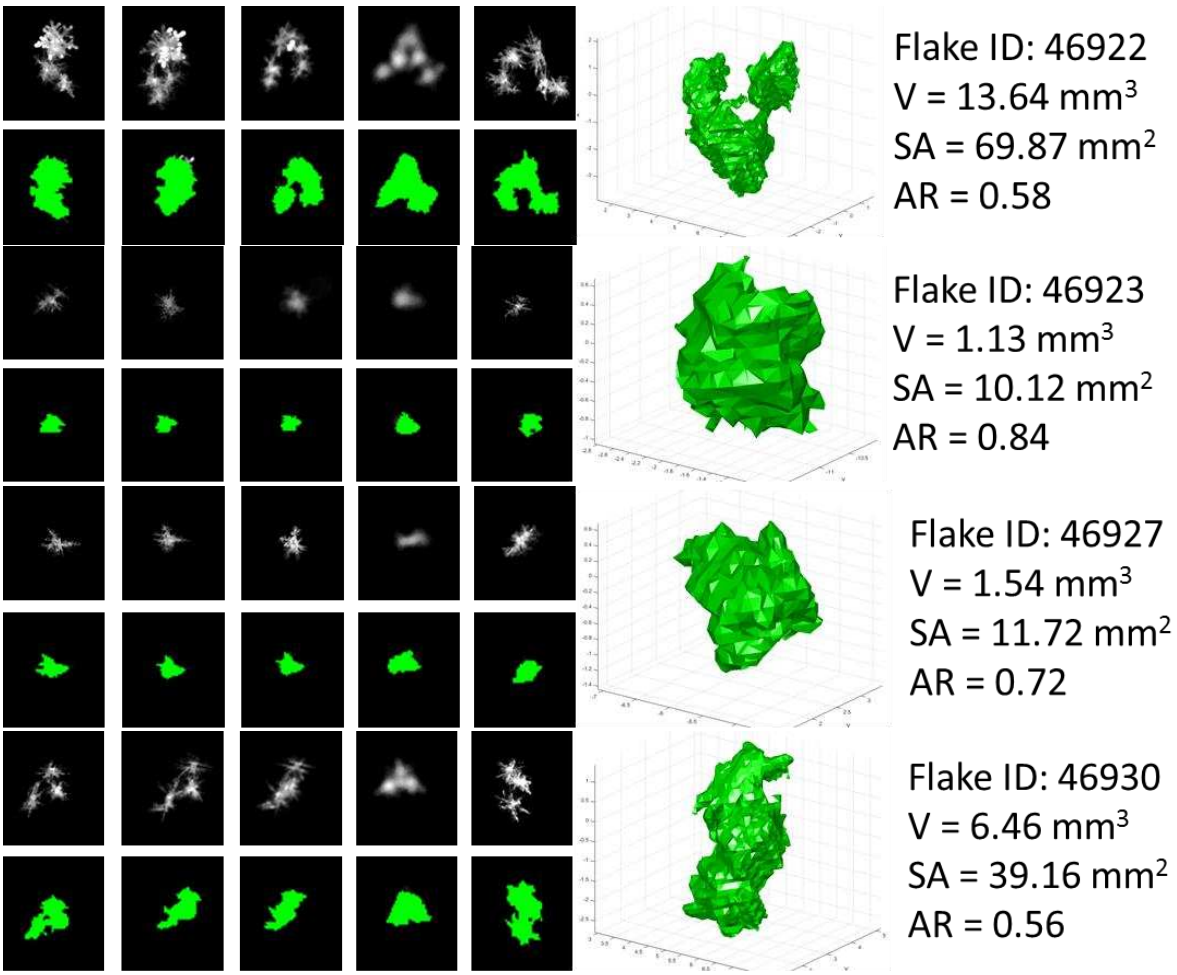

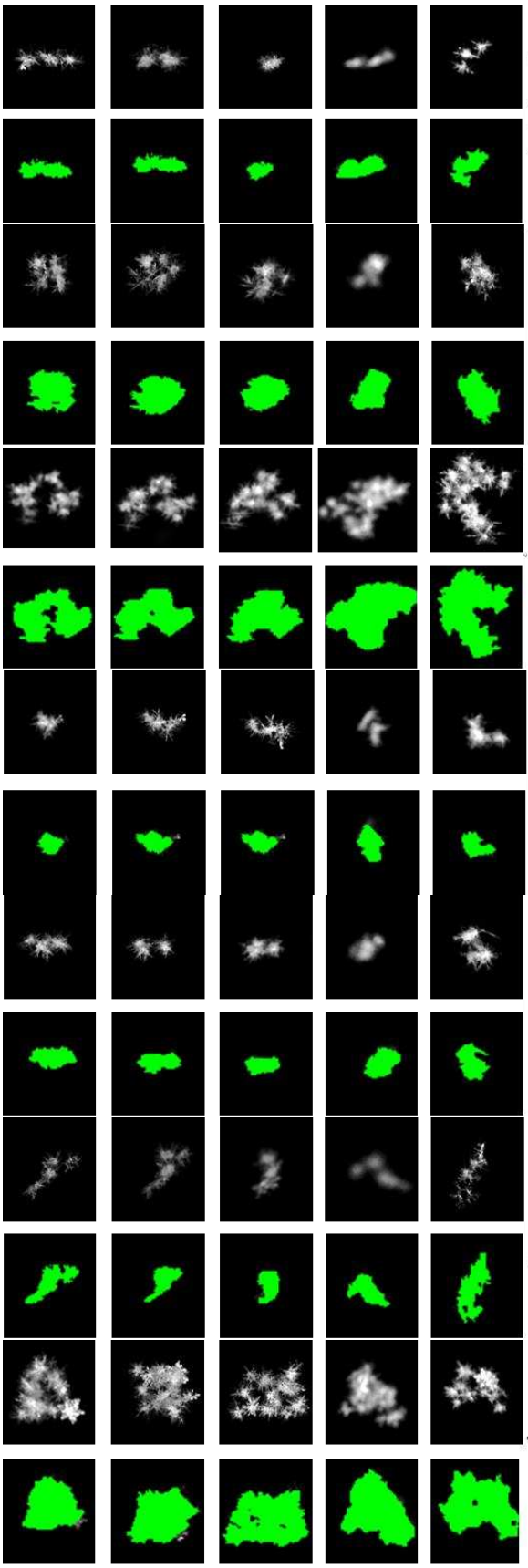

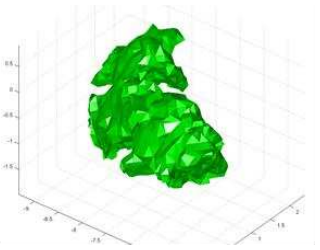

Flake ID: 46934
V = 3.54 mm^3
SA = 25.86 mm^2
AR = 0.50

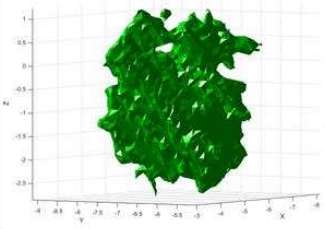

Flake ID: 46939
V = 13.71 mm^3
SA = 57.43 mm^2
AR = 0.75

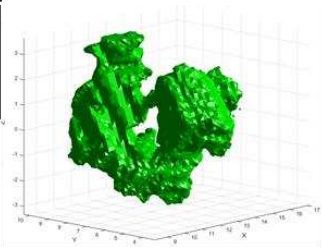

Flake ID: 46940
V = 53.67 mm^3
SA = 164.50 mm^2
AR = 0.78

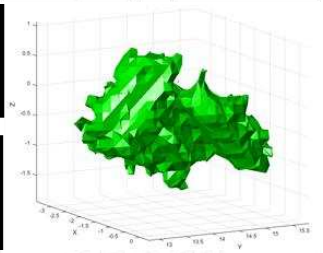

Flake ID: 46941
V = 3.51 mm^3
SA = 22.37 mm^2
AR = 0.65

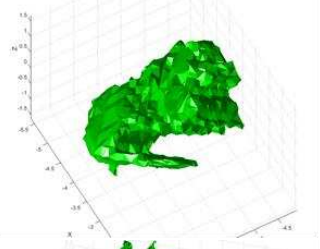

Flake ID: 46945
V = 5.20 mm^3
SA = 29.11 mm^2
AR = 0.74

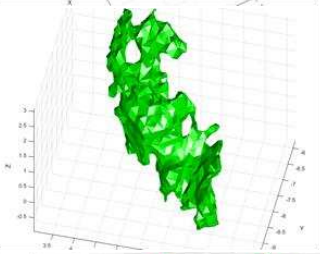

Flake ID: 46946
V = 4.52 mm^3
SA = 35.23 mm^2
AR = 0.45

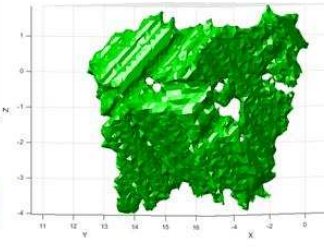

Flake ID: 46954
V = 52.33 mm^3
SA = 157.05 mm^2
AR = 0.81

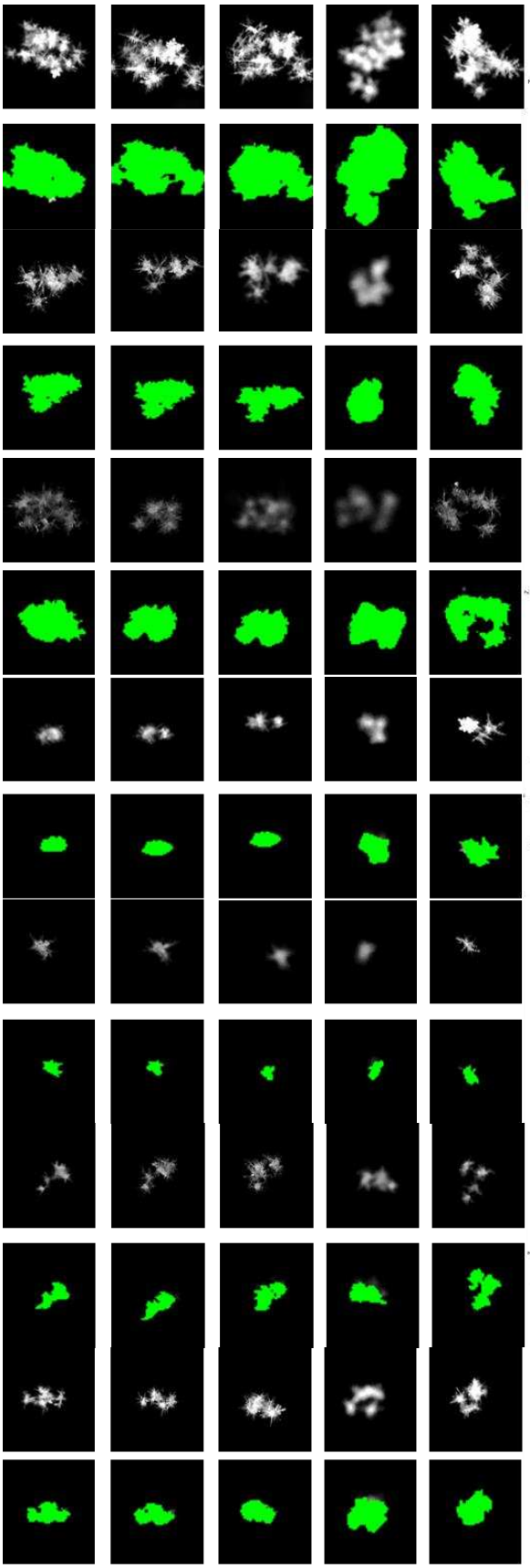

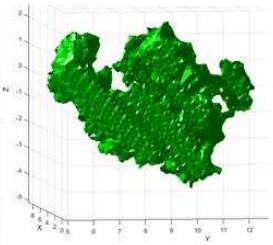

Flake ID: 46955
V = 59.61 mm^3
SA = 175.19 mm^2
AR = 0.69

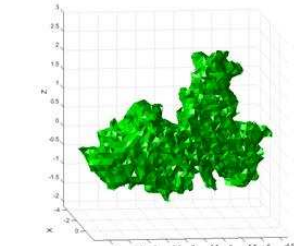

Flake ID: 46957
V = 13.42 mm^3
SA = 71.46 mm^2
AR = 0.67

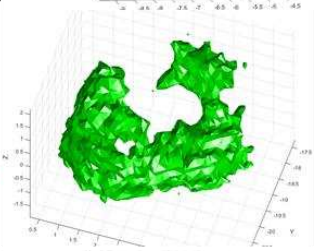

Flake ID: 46960
V = 20.78 mm^3
SA = 99.74 mm^2
AR = 0.78

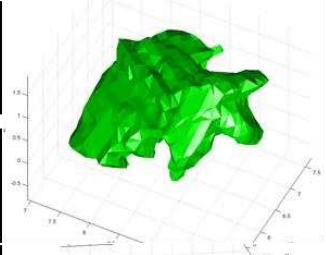

Flake ID: 46964
V = 4.34 mm^3
SA = 20.06 mm^2
AR = 0.64

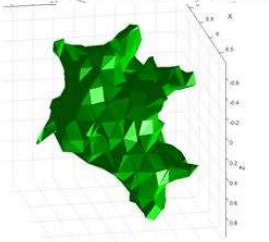

Flake ID: 46971
V = 0.71 mm^3
SA = 6.21 mm^2
AR = 0.71

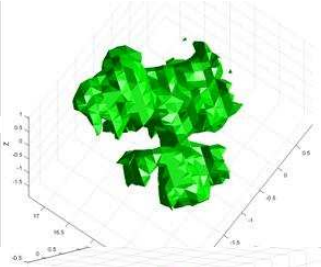

Flake ID: 46980
V = 2.58 mm^3
SA = 22.07 mm^2
AR = 0.64

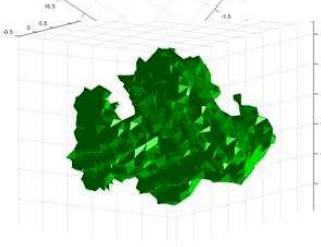

Flake ID: 46989
V = 6.39 mm^3
SA = 33.75 mm^2
AR = 0.75

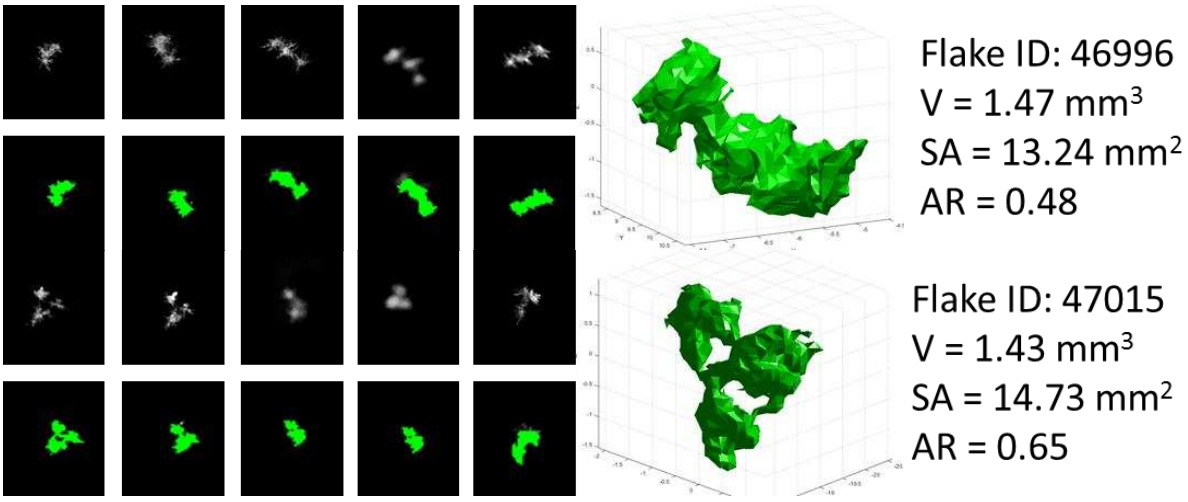

Figure 20. VH 3D Reconstruction Results: 20 examples of 3D visual hull reconstructions of different snowflakes collected at the MASCRAD Field Site (Fig. 1) during a February 23rd, 2015 snow event. For each snowflake, the five photographs from the modified MASC system (Fig. 2) are shown along with the 3D reconstructed shape triangular mesh and its back projections onto the original images. To the right of each 3D reconstruction, the calculated volume (V), surface area (SA), and aspect ratio (AR) of the mesh are given as well.

Figure 21 shows illustrative results of the MASC/visual-hull/meshing/scattering observation/analysis methodology and codes for an individual snowflake captured during a snow storm on February 21st, 2015 at the MASCRAD Field Site. As can be seen, the computed LDR and Z_{dr} single-particle values (given just for illustration) agree well with those measured simultaneously by the CSU-CHILL radar. These results illustrate one of the end goals of using the visual hull method for 3D shape reconstructions of snow and ice particles.

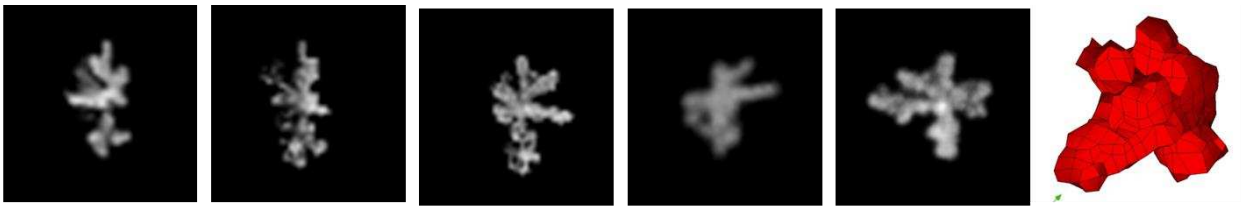

Scattering LDR = -31 dB Scattering Zdr = -0.1 dB Dielectric Constant: 1.216 - j0.0002

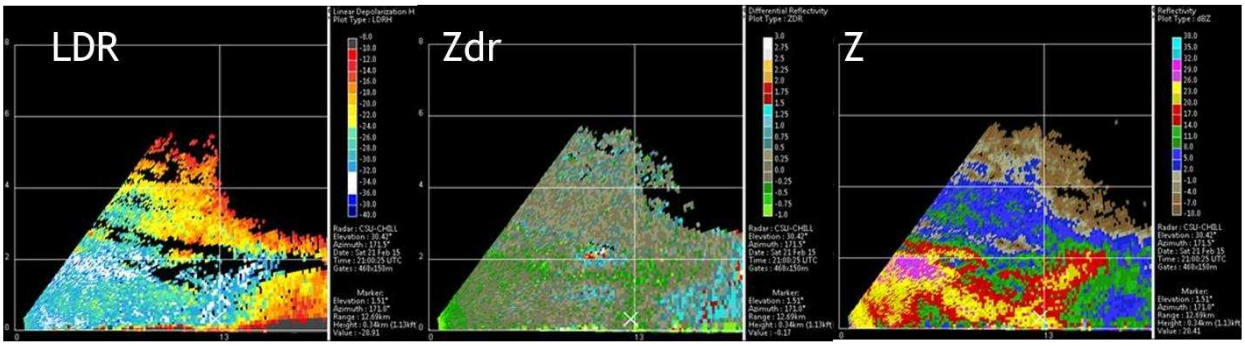

Radar LDR : -29 dB Radar Zdr : -0.17 dB Radar Z : 20 dBz

Figure 21. Scattering Results: Illustrative results of MoM-SIE scattering calculations based on the MASC (Figure 2) images of a snowflake captured at the MASCRAD Field Site (Figure 1) during a snow event on February 21st, 2015 and the resulting visual hull 3D shape reconstruction, in comparison with the corresponding CSU-CHILL radar range height indicator (RHI) plots of LDR and Z_{dr} at the same time. The site is at the 12.92-km range from the radar (white "×" marker in the plots).

7. Conclusions

This paper has proposed and presented a visual hull method and technique for reconstruction of realistic 3D shapes of snowflakes and other hydrometeors based on high-resolution photographs of particles in freefall from multiple views captured by a multi-angle snowflake camera, or another similar instrument, and the corresponding 2D silhouettes of an object. The 3D reconstructed snowflakes, represented by fine surface meshes of flat triangular patches, enable realistic computation of "particle-by-particle" scattering matrices, and can as well be used for studies of snow habits, for advanced analyses of microphysical characteristics of particles, and for particle classifications. They capture a large amount of detail about the hydrometeor shape that simple approximations miss. Hydrometeor shapes vary greatly from snowflake to snowflake during a winter event as has been shown in the results section. The visual hull method captures all of these variations and gives a set of reconstructions that adequately represent the snowflakes present at any point during the storm.

Preprocessing steps aimed to ensure quality 3D reconstructions such as the background removal and handling of multiple-snowflake images have been described. With the implementation of image processing techniques, lighting conditions that vary throughout the day and night have no effect on whether or not reconstructions of hydrometeors can be made. An improved mechanical calibration procedure of the MASC system has been created, using one calibration grid completely visible to all five cameras of the system simultaneously, instead of a standard procedure with a target grid being moved between the cameras separately. A technique for five-camera software self-calibration of the MASC system has been developed, to generate the projection matrices, internal and external parameter matrices, and a corrected position matrix,

which is input into the visual hull code in order to correct for the non-perfect mechanical calibration. The image processing techniques employed in conjunction with the software calibration also allow for images that contain multiple snowflakes to be used instead of being thrown out due to mismatch problems previously encountered. The resulting visual hull code works for all types of snowflakes that the MASC can adequately image. The process has been completely automatized and streamlined from the handling of the MASC images, to the visual hull method and the creation of meshes that adequately represent features of the geometry, to the estimation of the dielectric constant, and finally the scattering analysis.

The results have shown an ability of the proposed and presented visual hull method to successfully and accurately perform 3D reconstruction for snowflakes of very realistic, complicated, and diverse shapes and compositions, and very different sizes and complexities – collected at the MASCRAD Field Site, near Greeley, Colorado. The experiments have included demonstrations and evaluations of the improvement achieved by adding the two upper "external" cameras to the three original, "internal", MASC cameras. Tests have been carried out of the accuracy of visual hull 3D reconstructions based on simulated images of a sphere, of a known diameter, as well as on images of 3D printed fake snowflakes of complicated shapes created using 3D CAD modeling, dropped through the improved five-camera MASC, where it is possible to perform comparisons between the volume, surface area, and aspect ratio of the reconstructions and the respective values of the 3D CAD models of 3D printed snowflakes. Very good results of the visual hull shape reconstruction have been observed in all cases, including excellent coverage of the 2D back projections of the 3D reconstructed geometries as silhouettes onto the original snowflake images. All the results, in addition to demonstrating the power of the visual hull approach, have confirmed – in experiments involved in real snow storm observations

and those with simulated and fake 3D printed snowflakes – availability of sufficient silhouette information from the five cameras of the modified MASC system for 3D reconstruction and excellent mechanical and software self-calibration of the system.

This is the first time accurate realistic reconstructions of 3D hydrometeor shapes of winter precipitation based on high-resolution photographs of real (measured) snowflakes are performed. When compared to other existing methods and techniques for generating geometrical and physical models of the winter precipitation particles based on observations by advanced optical imaging disdrometers, the results presented in this paper are clearly much better than any snowflake 3D realistic-shape reconstruction data in the literature. In particular, when compared to the work in Teschl et al., the horizontal resolution of the 2DVD for the current production model is 150 µm, which is not sufficient to resolve details of the complexity of ice particles in winter precipitation, and there is, of course, a distinct advantage in obtaining photographs relative to the 2DVD contours [26]. The MASC camera resolution is three or more times higher than the 2DVD resolution and the MASC also has more angles of view, and both these facts allow for the visual hull method to provide more detailed reconstructions than the method used by Teschl et al. [26]. For the similar reasons, the MASC/visual hull approach is substantially advantageous over the ellipsoid models of snow particles obtained from 2DVD contour images in Huang et al. [27]. When compared to the work in Garret et al., by use of the visual hull method, all the images in a set together are related and a reconstruction that conforms to all the different angular views of the snowflake is created [25]. This provides a much more accurate 3D reconstruction of the snowflake than the model obtained by extruding the 2D silhouette of a single MASC image in Garret et al. [25].

Future work will include MASC/visual-hull/meshing/scattering analyses of data collected at multiple snow events observed at the MASCRAD Field Site, as well as the use of the 3D shape reconstructions of hydrometeors by the visual hull technique, in conjunction with the MASC instrument, for studies of snow habits, for advanced analyses of microphysical characteristics of particles, for hydrometeor classification, and for improvement of the radar-based estimation of liquid equivalent snow rates.

8. References

1. Pruppacher, H. R. and Klett, J. D., 2010: Microphysics of Clouds and Precipitation. (Second revised and expanded edition) *Series: Atmospheric and Oceanographic Sciences Library*, Vol. 18, *Springer*.

2. Mason, B. J., 2010: The Physics of Clouds. *Oxford University Press*.

3. Straka, J., D. S. Zrnić, and A. V. Ryzhkov, 2000: Bulk hydrometeor classification and quantification using polarimetric radar data: Synthesis of Relations. *J. Appl. Meteor.*, vol. **39**, 1341–1372.

4. Matrosov, S. Y., C. Campbell, D. Kingsmill, and E. Sukovich, 2009: Assessing Snowfall Rates from X-Band Radar Reflectivity Measurements. *J. Atmos. Oceanic Technol*., vol. **26**, 2324–2339.

5. Zhang, G., S. Luchs, A. Ryzhkov, M. Xue, L. Ryzhkova, and Q. Cao, 2011: Winter Precipitation Microphysics Characterized by Polarimetric Radar and Video Disdrometer Observations in Central Oklahoma. *J. Appl. Meteor. Climatol*., vol. **50**, 1558–1570.

6. Du, J., J. Shi, and H. Rott, 2010: Comparison between a multi-scattering and multi-layer snow scattering model and its parameterized snow backscattering model. *Remote Sensing of Environment*, vol. **114**, 1089–1098

7. Tyynelä, J., J. Leinonen, D. Moisseev, and T. Nousiainen, 2011: Radar Backscattering from Snowflakes: Comparison of Fractal, Aggregate, and Soft Spheroid Models. *J. Atmos. Oceanic Technol*., vol. **28**, 1365–1372.

8. Vivekanandan, J., V. N. Bringi, M. Hagen, and P. Meischner, 1994: Polarimetric radar studies of atmospheric ice particles. *Trans. IEEE Geosci Remote Sens*, vol. **32**, No. 1, 1−10.

9. Matrosov, S. Y., R. F. Reinking, R. A. Kropfli, B. E. Martner, and B. W. Bartram, 2001: On the Use of Radar Depolarization Ratios for Estimating Shapes of Ice Hydrometeors in Winter Clouds. *J. Appl. Meteor*., vol. **40**, 479–490.

10. Reinking, R. F., S. Y. Matrosov, R. A. Kropfli, and B. W. Bartram, 2002: Evaluation of a 45° Slant Quasi-Linear Radar Polarization State for Distinguishing Drizzle Droplets, Pristine Ice Crystals, and Less Regular Ice Particles. *J. Atmos. Oceanic Technol*., vol. **19**, 296–321.

11. Kennedy, P. C. and S. A. Rutledge, 2011: S-Band Dual-Polarization Radar Observations of Winter Storms. *J. Appl. Meteor. Climatol*., vol. **50**, 844–858.

12. Andrić, J., M. R. Kumjian, D. S. Zrnić, J. M. Straka, and V. M. Melnikov, 2012: Polarimetric signatures above the melting layer in winter storms: An observational and modeling study. Early on-line release, *Journal of Applied Meteorology and Climatology*, doi: http://dx.doi.org/10.1175/JAMC-D-12-028.1

13. Kim, M. J., 2006: Single scattering parameters of randomly oriented snow particles at microwave frequencies, *Journal of Geophysical Research*, col. 111, D14201, doi:10.1029/2005JD006892.

14. Ishimoto, H., 2008: Radar Backscattering Computations for Fractal-Shaped Snowflakes. *Journal of the Meteorological Society of Japan*, vol. **86**, 459-469.

15. Kneifel, S., U. Löhnert, A. Battaglia, S. Crewell, and D. Siebler, 2010: Snow scattering signals in round based passive microwave radiometer measurements. *Journal of Geophysical Research*, vol. **115**, D16214, doi:10.1029/2010JD013856.

16. Kim, M., M. Kulie, C. O'Dell, and R. Bennartz, 2007: Scattering of ice particles in microwave frequencies: A physically based parameterization. *J. Appl. Meteor. Climatol.*, vol. **46**, 615–633.

17. Hong, G., 2007a: Parameterization of scattering and absorption properties of nonspherical ice crystals at microwave frequencies, *Journal of Geophysical Research*, vol. **112**, D11208, doi:10.1029/2006JD008364.

18. Liu, G., 2010: Approximation of Single Scattering Properties of Ice and Snow Particles for High Microwave Frequencies. *Journal of the Atmospheric Sciences*, vol. **61**, 2441-2456.

19. Evans, K. F., and G. Stephens, 1995: Microwave radiative transfer through clouds composed of realistically shaped ice crystals. Part I: Single scattering properties. J. *Atmos. Sci.*, vol. **52**, 2041–2057

20. Hong, G., 2007b: Radar backscattering properties of nonspherical ice crystals at 94 GHz. *J. Geophys*. Res., vol. **112**, D22203. doi:10.1029/2007JD008839.

21. Grecu, M., and W. Olson, 2008: Precipitating snow retrievals from combined airborne cloud radar and millimeter-wave radiometer observations. *J. Appl. Meteor. Climatol*., vol. **47**, 1634–1650.

22. Kuo, K., W. Olson, B. Johnson, M. Grecu, L. Tian, T. Clune, B. van Aartsen, A. Heymsfield, L. Liao, and R. Meneghini, 2016: The Microwave Radiative Properties of Falling Snow Derived from Nonspherical Ice Particle Models. Part I: An Extensive Database of Simulated Pristine Crystals and Aggregate Particles, and Their Scattering Properties. *Journal of Applied Meteorology and Climatology,* vol. **55**, 691-708.

23. Ryzhkov, A. V., D. S. Zrnic, and B. A. Gordon, 1998: Polarimetric Method for Ice Water Content Determination. *J. Appl. Meteor*., vol. **37**, 125–134.

24. Barthazy, E., S. Göke, R. Schefold, and D. Högl, 2004: An optical array instrument for shape and fall velocity measurements of hydrometeors. *J. Atmos. Oceanic Technol*., vol. **21**, 1400–1416.

25. Garrett, T. J., C. Fallgatter, K. Shkurko, and D. Howlett, 2012: Fallspeed measurement and high-resolution multi-angle photography of hydrometeors in freefall. *Atmos. Meas. Tech. Discuss*., vol. **5**, 4827−4850, doi:10.5194/amtd-5-4827-2012.

26. Teschl, F., W. L. Randeu, and M. Schönhuber, 2006: Modelling microwave scattering by solid precipitation particles. *Proceedings of The European Conference on Antennas and Propagation: EuCAP 2006*, Nice, France, 310.1−310.5.

27. Huang, G., V. N. Bringi, D. Moisseev, W. A. Petersen, L. Bliven, and D. Hudak, 2014: Use of 2D-Video Disdrometer to Derive Mean Density-Size and Ze-SR Relations: Four Snow Cases from the Light Precipitation Validation Experiment. *Atmospheric Research,* vol. **153**, 34-48.

28. Böhm, H. P., 1989: A general equation for the terminal fall speed of solid hydrometeors. *J. Atmos. Sci*., vol. **46**, 2419–2427.

29. Chobanyan E., N. J. Sekeljiic, A. B. Manic, M. M. Ilic, V. N. Bringi, and B. M. Notaros, 2015: Efficient and Accurate Computational Electromagnetics Approach to Precipitation Particle Scattering Analysis Based on Higher Order Method of Moments Integral-Equation Modeling. *J. Atmos. Oceanic Technol.*, vol. **32**, 1745–1758.

30. Notaros B., V. N. Bringi, C. Kleinkort, G.-J. Huang, E. Chobanyan, M. Thurai, O. Notaros, A. Manic, A. Newman, P. Kennedy, J. Hubbert, T. Lim, W. Brown, and M. Ilic, 2015a: Measurement and Characterization of Winter Precipitation at MASCRAD Snow Field Site. *Proceedings of the 2015 IEEE International Symposium on Antennas and Propagation and North American Radio Science Meeting*, July 19-25, 2015, Vancouver, BC, Canada.

31. Notaros, B. M., V. N. Bringi, A. J. Newman, C. Kleinkort, G.-J. Huang, P. Kennedy, and M. Thurai, 2015b: Accurate Characterization of Winter Precipitation Using In-Situ Instrumentation, CSU-CHILL Radar, and Advanced Scattering Methods. *2015 AGU Fall Meeting*, 14-18 December 2015, San Francisco, CA.

32. Kennedy, P. C., C. Kleinkort, G.-J. Huang, M. Thurai, A. Newman, J. Hubbert, S. Rutledge, V. N. Bringi, and B. M. Notaros, 2015: Preliminary Results from the Multi-Angle Snowflake Camera and Radar (MASCRAD) Project. *American Meteorological Society's 37th Conference on Radar Meteorology*, 14-18 September, 2015, Norman, OK.

33. Bringi, V. N., B. Notaros, C. Kleinkort, G.-J. Huang, M. Thurai, and P. Kennedy, 2015: Comprehensive Analysis of an Unusual Winter Graupel Shower Event Recorded by an S-Band Polarimetric Radar and Two Optical Imaging Surface Instruments. *American Meteorological Society's 37th Conference on Radar Meteorology*, 14-18 September, 2015, Norman, OK.

34. Kleinkort, C., G.-J. Huang, E. Chobanyan, A. Manic, M. Ilic, A. Pezeshki, V. N. Bringi, and B. Notaros, 2015a: Visual Hull Method Based Shape Reconstruction of Snowflakes from MASC Photographs. *Proceedings of the 2015 IEEE International Symposium on Antennas and Propagation and North American Radio Science Meeting*, July 19-25, 2015, Vancouver, BC, Canada.

35. Kleinkort, C., G.-J. Huang, S. Manic, A. Manic, P. Kennedy, J. Hubbert, A. Newman, V. N. Bringi, and B. Notaros, 2015b: 3D Shape Reconstruction of Snowflakes from Multiple Images, Meshing, Dielectric Constant Estimation, Scattering Analysis, and Validation by Radar Measurements. *American Meteorological Society's 37th Conference on Radar Meteorology*, 14-18 September, 2015, Norman, OK.

36. Laurentini, A., 1994: The visual hull concept for silhouette-based image understanding. *IEEE Transaction on Pattern Analysis and Machine Intelligence*, vol. **16**, no. 2, 150−162.

37. VHMC Software: Visual Hull Mesh Code, 2012: http://www.dip.ee.uct.ac.za/~kforbes/DoubleMirror/DoubleMirror.html

38. Bloomenthal, J., 1994: An Implicit Surface Polygonizer, The University of Calgary, Calgary, Alberta T2N 1N4 Canada.

39. Forbes, K., 2007: Calibration, recognition, and shape from silhouettes of stones. *PhD thesis, Department of Electrical Engineering, University of Cape Town*, Cape Town, South Africa.

40. Bader, M. MB – Ruler the Triangula Screen Ruler, http://www.markus-bader.de/MB-Ruler/index.php.

41. Newman, A. J., P. A. Kucera, and L. F. Bliven, 2009: Presenting the Snowflake Video Imager (SVI), *Journal of Atmospheric and Oceanic Technology*, vol. **26**:2, 167-179.

42. Svoboda, T., Martinec, D. and Pajdla, T., A convenient multi-camera self-calibration for virtual environments., PRESENCE: *Teleoperators and Virtual Environments*, vol. **14**, (4), pp 407-422, August 2005. MIT Press.

43. Strurm, P., B. Triggs, 1996: A Factorization Based Algorithm for Multi-Image Projective Structure and Motion. *4th European Conference on Computer Vision*, Cambridge, England, 709-720.

44. Notaros, B. M., V. N. Bringi, E. Chobanyan, C. Kleinkort, S. B. Manic, N. J. Sekeljic, A. B. Manic, and M. M. Ilic, 2015c: Computation of Particle Scattering Matrices and Polarimetric Radar Variables for Winter Precipitation Using T-Matrix Method, DDA Method, and Higher Order MoM-SIE Method. *American Meteorological Society's 37th Conference on Radar Meteorology*, 14-18 September, 2015, Norman, OK.

45. Djordjevic, M. and B. M. Notaros, 2004: Double higher order method of moments for surface integral equation modeling of metallic and dielectric antennas and scatterers. *IEEE Transactions on Antennas and Propagation*, vol. **52**, no. 8, 2118−2129.

46. ANSYS ICEM CFD, 2014: http://resce.ansys.com/Products/Other+Products/ANSYS+ICEM+CFD